Molecular Insights into Cross-Species Spillover of Coronavirus HKU5 via ACE2 Receptor Recognition

Lingyun Xia[1,2,3†], Yuanyuan Zhang[1,2,3†], Yuya Li[1,2,3†], Dexin Li[1,2,3], Qiang Zhou[1,2,3*]

[1]Center for Infectious Disease Research, Research Center for Industries of the Future, Zhejiang Key Laboratory of Structural Biology, School of Life Sciences, Westlake University, Hangzhou, Zhejiang, 310024, China.

[2]Westlake Laboratory of Life Sciences and Biomedicine, Hangzhou, Zhejiang, 310024, China.

[3]Institute of Biology, Westlake Institute for Advanced Study, Hangzhou, Zhejiang, 310024, China.

[†]These authors contributed equally to this work.

[*]Corresponding author. Email: zhouqiang@westlake.edu.cn

Abstract

Coronaviruses represent a significant zoonotic threat, with host adaptation serving as a pivotal determinant of cross-species transmission. The bat-derived β-coronavirus HKU5 utilizes its spike (S) protein for receptor recognition and viral entry. Here, we report the cryo-electron microscopy (cryo-EM) structure of the HKU5 S protein in a closed conformation. Two fatty acids are bound to the HKU5 S protein, stabilizing the S protein in the closed conformation. Furthermore, we solve the structure of the HKU5 receptor-binding domain (RBD) in complex with the peptidase domain (PD) of *Pipistrellus abramus* angiotensin-converting enzyme 2 (ACE2), uncovering a unique binding mode distinct from other coronaviruses that use ACE2 as their receptor. Evolutionary and functional analyses indicate that mutations on RBD can modulate receptor binding, while conservation and structural modeling suggest that HKU5 has the potential to cross species barrier. Notably, we identify ACE2 orthologs in avian species, such as *Pitta sordida*, that support stable HKU5 RBD binding and interaction. These findings provide molecular insights into the host adaptation of HKU5 and underscore the importance of surveillance for this virus and its zoonotic risk.

Introduction

Coronaviruses (CoVs) are zoonotic pathogens with significant potential for cross-species transmission, exemplified by SARS-CoV[1], MERS-CoV[2] and SARS-CoV-2[3,4]. They often originate from animal reservoirs, especially bats, before spilling over to humans[5-7]. The spike (S) protein of coronaviruses mediates receptor recognition and membrane fusion, with the receptor-binding domain (RBD) typically determining host specificity and spillover potential[8,9]. The RBD can adopt "up" or "down" conformation, where only the "up" state engages receptors[10-12]. These conformational shifts are regulated by various factors, including sialic acids and fatty acids[13-17].

Bat coronavirus HKU5 (BatCoV-HKU5) belongs to the β-coronavirus Merbecovirus lineage and is closely related to MERS-CoV[18-20]. Despite being discovered in 2006 and the identification of numerous related sublineages[21], HKU5 remains relatively underexplored compared to pandemic coronaviruses. Recent studies have shown that HKU5 can utilize the angiotensin-converting enzyme 2 (ACE2) from *Pipistrellus abramus* for host cell entry[22], which serves as a receptor for multiple human coronaviruses, including SARS-CoV[23], SARS-CoV-2[4,24], and HCoV-NL63[25], and has been implicated in repeated spillover events[26].

In this work, we solved the cryo-electron microscopy (cryo-EM) structure of the HKU5 S protein in a closed conformation, which are bound with two fatty acids that can stabilize the close conformation of the S protein. We also characterize the interaction between HKU5 RBD and bat ACE2, noting differences from MERS-CoV and SARS-CoV-2. By integrating structural analysis, evolutionary insights, and functional assessment of RBD mutation, we provide a comprehensive perspective on HKU5's host adaptability and spillover risk. These

55 findings contribute valuable knowledge to coronavirus research and highlight the need for
56 ongoing surveillance of HKU5 and related viruses.
57
58 **Results**
59 **Structure of HKU5 S protein in closed conformation**
60 We have over-expressed and purified the HKU5 S protein, and then solved its cryo-EM
61 structure at a resolution of 2.4 Å (Supplementary information, Fig. S1). Unlike the open
62 conformations observed in the S proteins of SARS-CoV-2[11], MERS-CoV[27] or HKU1-B[28], all
63 three RBDs of the HKU5 S protein are in the "down" position (Fig. 1a). This closed
64 conformation hinders interactions with host receptors, potentially delaying host cell entry or
65 facilitating immune evasion[14,29].
66 In the cryo-EM map of the HKU5 S protein, two additional non-protein densities were
67 identified for each protomer. The first one is in a pocket (pocket 1) near the interface between
68 the RBDs of adjacent protomers. And the second one is in another pocket within the RBD
69 (pocket 2), near the receptor-binding motif (RBM) (Fig. 1a). Mass spectrometry experiments
70 suggest the HKU5 S protein contains oleic acid and palmitic acid (Figs. 1b, c and
71 Supplementary information, Fig. S2), which were fitted to pocket 1 and 2 based on the density
72 shape, respectively (Fig. 1a). The pocket 1 is formed by hydrophobic residues F393, L419,
73 L422, L423, F426, V428, F431, P438, L441, L449, V451, V488, A490, F569 and V571 on the
74 RBD (Fig. 1d). The polar head of oleic acid interacts with residues Y463, S468 and A469 from
75 an adjacent protomer (Fig. 1d). In cryo-EM map of the HKU5 S protein with S468A&Y463A
76 double mutant (S_{DM} protein), the density corresponding to oleic acid was absent, indicating the

77 importance of these polar residues for the interaction with oleic acid (Supplementary
78 information, Fig. S3, 4). Compared to the wild-type (WT) protein, the S_{DM} protein exhibited a
79 ~5° clockwise rotation of the N-terminal domain (NTD) (Supplementary information, Fig. S4,
80 b andSupplementary information, Video S1), resulting in a looser trimeric assembly[30].
81 Additionally, the SD1 and SD2 domain shifted away from RBD toward NTD, forming new
82 polar interactions such as a salt bridge between R689 of SD2 and D346 of NTD, and a hydrogen
83 bond network involving residues ^{689}RMT^{691} of SD2 and ^{348}GYDD^{351} of NTD (Supplementary
84 information, Fig. S4d and Supplementary information, Video S2). These changes were
85 accompanied by structural remodeling, suggesting that oleic acid is beneficial for maintaining
86 the closed conformation of the S protein. This observation parallels findings in SARS-CoV-2,
87 where linoleic acid binding stabilizes the closed state of its S protein[17]. The presence of oleic
88 acid in HKU5 S protein suggests a conserved mechanism to regulate S protein conformational
89 dynamics, modulating receptor binding and pre-fusion activation to optimize viral entry
90 efficiency.
91 The pocket 2, where the palmitic acid binds, is in the interior of RBD (Fig. 1e), which has not
92 been reported in any other S protein of coronaviruses. Although the pocket 2 is close to the
93 receptor-binding interface, it does not directly contact it, possibly suggesting a structural or
94 regulatory role in modulating RBD dynamics rather than directly influencing ACE2 binding.
95
96 **Interaction of HKU5 RBD with bat ACE2**
97 To elucidate the interaction between the HKU5 S protein and the ACE2 receptor of its natural
98 host, *Pipistrellus abramus*, we conducted biochemical and structural studies. Gel filtration

99 chromatography revealed that the S protein in its closed conformation does not co-migrate with
100 the peptidase domain (PD) of the *Pipistrellus abramus* ACE2 (*Pa*PD), indicating that the S
101 protein in closed conformation cannot directly bind to the receptor (Supplementary information,
102 Fig. S5). To understand the molecular mechanism underlying HKU5 S protein receptor
103 recognition, we determined the cryo-EM structure of the HKU5 RBD in complex with *Pa*PD
104 at a resolution of 3.2 Å, allowing accurate modeling and analysis (Fig. 2a and Supplementary
105 information, Fig. S6).
106 The RBM of the HKU5 RBD adopts a compact super-secondary structure comprising a four-
107 stranded anti-parallel β-sheet (β5~β8, residues N504~P560) and a short helix (α4, residues
108 S457~L464), which are critical for receptor recognition and binding (Figs. 2a, b). The *Pa*PD
109 comprises key structural elements that facilitate its interaction with HKU5 RBD, including the
110 α1 helix (18~54 a. a.), α2 helix (90~101 a. a.), α3 helix (322~330 a. a.), a β-hairpin (346~358
111 a. a.), and a loop region (L_A; 318~330 a. a.) (Figs. 2a, b).
112 The interface between the RBD and *Pa*PD spans ~1107 Å² area and can be divided into three
113 distinct contact patches, each playing a pivotal role in stabilizing the complex. The patch 1
114 region involves interactions between RBD residues from β5 and β6 (E510, Y512, A516, Y517,
115 G518, K519, Y521) and *Pa*PD residues in the α1 helix (R26, E37), α2 helix (D90, N96), β-
116 hairpin (N353), and loop region L_A (N386, S388) (Fig. 2c). The interaction is mediated by eight
117 hydrogen bonds and one salt bridge (Fig. 2c), which collectively ensure the stability of this
118 initial contact point. The predominance of polar and charged residues highlights the importance
119 of this region in the high-affinity binding observed in the HKU5 RBD–*Pa*PD complex. The
120 residues of patch 2 from β7 and β8 of the RBD (K543, Y544, S546, Y557) interact with *Pa*PD

residues from the α1 helix (N38), α3 helix (D329), and β-hairpin (D354, K352) (Fig. 2d). Notably, K543 and Y557 form a salt bridge and a hydrogen bond with D329, respectively, while Y544 interacts with D354 and K352. N38 and K352 also engage with S546, forming the primary hydrogen bond network in this patch (Fig. 2d). These interactions ensure the structural stability of this secondary contact region. Patch 3 incorporated a variety of stabilizing interactions, such as a cation-π interaction, a salt bridge, and hydrophobic interactions. Specifically, residue Y559 in RBD β8 forms a cation-π interaction with R328 in the *Pa*PD L_A loop, while residue D459 in RBM and residue R328 in *Pa*PD form a salt bridge. Additionally, hydrophobic interactions are observed in the region encompassing Y463 of the RBD α4 loop, Y507 of β1, and P324 of the *Pa*PD α3 helix. These interactions synergistically contributed to the enhanced stability of the complex (Fig. 2e). Collectively, these three patches establish a highly specific binding interface between the HKU5 RBD and *Pa*PD, which is crucial for host ACE2 recognition and initiation of viral entry.

In addition to HKU5, numerous other coronaviruses utilize ACE2 for host cell entry, including the epidemic- or pandemic-causing SARS-CoV[23] and SARS-CoV-2[4,24], as well as human coronavirus HCoV-NL63[25] and several bat coronaviruses, such as NeoCoV[31], PDF-2180[31], PRD-0038[32], and MOW15-22[33]. The RBM of SARS-CoV-2 forms an accessible, expansive surface (residues 438~506) that tightly binds human ACE2 (Fig. 2f). The RBD of HCoV-NL63 features a β-sandwich core structure and comprises three non-contiguous RBMs, with binding sites concentrated centrally (Fig. 2f). The PDF-2180 RBM adopts a four-stranded anti-parallel β-sheet, resembling the HKU5 RBM, but latter displays a more compact conformation, with an extended fourth strand (Fig. 2f).

143 Structural comparison reveals differences of the HKU5 RBD-ACE2 interface to the other
144 coronaviruses (Fig. 2g). HKU5 shares partial binding footprints with the known modes of
145 SARS-CoV-2, HCoV-NL63, and PDF-2180, but lacks conserved residues among these viruses
146 (Fig. 2g). This indicates that the HKU5 RBD employs a unique interface to interact with ACE2,
147 likely contributing to the host specificity.
148

149 **Evolutionary dynamics of HKU5 RBD**

150 To explore the evolutionary dynamics of the HKU5 RBD, we performed a clustering analysis
151 on the sequences in the NCBI protein database sharing more than 80% identity with the HKU5
152 S protein (Supplementary information, Fig. S7). The results show that six HKU5 lineages
153 recorded in the NCBI Taxonomy database are distributed across two clusters (Supplementary
154 information, Fig. S7). Most of the HKU5 RBD residues are highly conserved across various
155 lineages, particularly within the core framework of RBD, indicating their critical role in
156 maintaining structural integrity (Supplementary information, Fig. S7, 8). However, over 30
157 mutation sites are found in RBM, particularly spanning the segment Q494~G564
158 (Supplementary information, Fig. S7, 8) that accounts for more than two-thirds of the residue
159 indels and point mutations.

160 To evaluate the impact of different HKU5 lineages on ACE2 recognition specificity, we
161 employed bio-layer interferometry (BLI) to quantify the *Pa*PD binding affinity of various
162 HKU5 RBD variants (Fig. 3a). The highest affinity is observed for HKU5, with a Kd of 19.94
163 ± 0.23 nM. BtPa-BetaCoV/GD2013 and BatCoV-HKU5-3 display similar binding affinity, at
164 23.40 ± 0.27 nM and 25.17 ± 0.29 nM, respectively. BatCoV-HKU5-related viruses show a

165 slightly lower affinity, with a Kd of 35.24 ± 0.37 nM. These HKU5 lineages exhibit *Pa*PD
166 binding affinity either comparable to or slightly lower than that of the HKU5, suggesting that
167 the mutations observed in these variants exert a mild effect on receptor binding.
168 To further investigate the influence of conserved interface residues on the interaction between
169 HKU5 RBD and *Pa*PD, we utilized a tripartite split-fluorescence system[34] in conjunction with
170 flow cytometry to identify potential key residues within the HKU5 RBD (Figs. 3b-c). These
171 assays showed high sensitivity for the interaction of the HKU5 RBD with *Pa*PD, with signal
172 intensity exceeding that of the HKU5 RBD with PD of *Homo sapiens* ACE2 (*Hs*PD), which is
173 a negative control, by more than tenfold (Fig. 3d). Targeted mutations of interface residues
174 revealed that, except for Y544, mutations of the other residues, namely Y463, Y507, Y517,
175 K519, Y521, K543, S546, Y557, and Y559, led to varying degrees of destabilization of the
176 interaction, as evidenced by decreased fluorescence (Fig. 3d). Notably, the K519A mutation
177 caused a reduction in fluorescence intensity by more than 50%. It is important to highlight that
178 residues Y507, K543, Y544, and Y557 are not highly conserved in the HKU5 (Fig. 3d). When
179 these non-conserved residues were mutated to their corresponding residues in other lineages,
180 we observed reduction in fluorescence intensity by approximately 50%, as in the cases of
181 Y507H, K543D, and Y557S (Fig. 3d). These findings contribute to a deeper understanding of
182 the factors influencing the binding affinity of the HKU5 virus for its receptor.

183 **Cross-species transmission risk analysis of HKU5**

184 To investigate the potential for cross-species transmission of HKU5, we conducted a detailed
185 structural analysis of the *Pa*PD residues recognized by HKU5. We introduced point mutations
186 in several polar residues of *Pa*PD that might maintain the interface interaction, including R26A,

187 E37A, Q96A, N321A, P324A, W327A, R328A, D329A, K352A, N353A, D354A, and S388A
188 (Fig. 4a). Tripartite split-fluorescence experiments performed on these mutants revealed that,
189 with the exception of E37 and Q96, most of the mutations resulted in the noticeable reduction
190 in relative fluorescence intensity, indicating their significant contribution to the virus-receptor
191 interaction (Fig. 4b). Notably, the R328A mutation in *Pa*PD caused a reduction in relative
192 fluorescence intensity to below 50%. The R328 in *Pa*PD stabilizes the interface through a salt
193 bridge with D459 in HKU5 RBD and a cation-π interaction with Y559 in HKU5 RBD, thus
194 maintaining the interaction between HKU5 and *Pa*PD (Fig. 2e). This result aligns with the
195 reduced fluorescence intensity observed in the HKU5 RBD Y559A mutant (Figs. 3d, 4b).
196 There are two consecutive three-residue motifs in *Pa*PD involved in interaction with HKU5
197 RBD, namely ^{327}WRD^{329} and ^{352}KND^{354}. Point mutation in these two motifs caused marked
198 reduction in fluorescence intensity (Fig. 4b). We hypothesize that the ^{327}WRD^{329} and ^{352}KND^{354}
199 motifs of *Pa*PD play a critical role in HKU5 receptor recognition. Sequence alignment of ACE2
200 from various species indicates that these motifs are conserved across multiple species, such as
201 an avian *Pitta sordida* (Supplementary information, Fig. S9). The sequence identity of the PD
202 of *Pitta sordida* ACE2 (*Ps*PD) with *Pa*PD and *Hs*PD is 69% and 76%, respectively (Fig. 4c).
203 The affinity of *Ps*PD for HKU5 RBD measured by BLI is 122.9 ± 1.3 nM (Fig. 4d).
204 To analyze the impact of the receptor interface residue changes on HKU5 RBD recognition,
205 we solved the cryo-EM structure of the HKU5 RBD–*Ps*PD complex. Perhaps due to the
206 reduced affinity, a large fraction of the *Ps*PD molecules remained unbound in the 2D
207 classification. However, after collecting sufficient data, we solved the cryo-EM structure of the
208 HKU5 RBD–*Ps*PD complex at a resolution of 3.2 Å (Fig. 4e and Supplementary information,

209 Fig. S10). *Ps*PD binds to the HKU5 RBD in a manner similar to *Pa*PD (Supplementary
210 information, Fig. S11a). The core interaction interface between *Ps*PD and HKU5 RBD is
211 maintained by the WRD and KND motifs in *Ps*PD, along with other conserved residues (Figs.
212 4f-i). Some interface residues of *Ps*PD were mutated relative to *Pa*PD, including Q25, D37,
213 E325, G387, and P389, which correspond to R26, N38, P324, N386, and S388 in *Pa*PD,
214 respectively (Fig. 4c). The E325 in *Ps*PD (corresponding to P324 in *Pa*PD) disrupts its
215 hydrophobic interaction with HKU5 RBD Y463 but forms hydrogen bond instead (Fig. 4i and
216 Supplementary information, Fig. S11b). The E325 in *Ps*PD forms a salt bridge with *Ps*PD R329
217 (corresponding to R328 in *Pa*PD), which causes a conformational shift of *Ps*PD R329,
218 disrupting the salt bridge between *Ps*PD R329 and the HKU5 RBD D459 (Fig. 4i and
219 Supplementary information, Fig. S11b). The R33 in *Ps*PD (corresponding to H34 in *Pa*PD)
220 forms new polar contacts with T514 and E551 of the HKU5 RBD. Additionally, N322 in *Ps*PD
221 shows noticeable glycosylation, which was not observed in *Pa*PD, forming new interactions at
222 the RBD–*Ps*PD interface (Supplementary information, Fig. S11d). However, compared to
223 *Pa*PD, the overall structure of *Ps*PD is slightly more distanced from the RBD domain
224 (Supplementary information, Fig. S11), disrupting certain polar interactions, such as between
225 *Pa*PD E37 and RBD K519 (Supplementary information, Fig. S11e).
226 To investigate whether different HKU5 subclades affect RBD binding to *Ps*PD, we measured
227 the Kd values of the RBD of BtPa-BetaCoV/GD2013, HKU5-3, and other HKU5-related
228 viruses for *Ps*PD, which were 137.8 ± 0.9 nM, 176.2 ± 1.4 nM, and 232.5 ± 2.0 nM,
229 respectively (Fig. 4d). These differences suggest that mutations in different HKU5 strains may

230 facilitate adaptation to ACE2 receptors from different species, potentially enabling cross-
231 species transmission.
232 We analyzed the conservation of the RBD binding interface on ACE2 between bats and human.
233 The results revealed substantial differences in the ^{327}WRD^{329} and ^{352}KND^{354} residues between
234 bat and human ACE2, which may limit the potential for HKU5 to bind to human ACE2 (Fig.
235 4c). Although the spillover risk of HKU5 to human is currently low, continuous monitoring is
236 warranted, especially in the context of viral evolution.
237 In summary, these findings provide a comprehensive perspective on the structural, functional,
238 and evolutionary characteristics of HKU5, enhancing our understanding of its receptor-binding
239 specificity and potential for cross-species transmission.
240

241 **Discussion**

242 This study provides critical insights into the molecular mechanisms underlying HKU5 S
243 protein interaction with ACE2, shedding light on its structural adaptations, evolutionary
244 dynamics, and the potential of cross-species transmission.
245 We identified two fatty acid molecules, oleic acid and palmitic acid, bound to the S protein of
246 HKU5. These molecules stabilize the closed conformation of the S protein, likely modulating
247 receptor accessibility. Similar to findings in other β-coronaviruses, including SARS-CoV-2[17]
248 and HCoV-OC43[35], fatty acid binding occurs at conserved hydrophobic pockets within the
249 RBD (Supplementary information, Table 1). Mutational analyses revealed that disruption of
250 these interactions in HKU5 induces a structural shift toward a more relaxed conformation. This
251 suggests that fatty acids play a crucial role in maintaining the closed state, potentially limiting

252 premature receptor binding and aiding immune evasion. Notably, we identified a novel fatty
253 acid binding pocket proximal to the RBM region in the HKU5 RBD. Cryo-EM map of the
254 HKU5 RBD–*Pa*PD complex does not contain density in this pocket, indicating that fatty acid
255 binding may require the trimeric structure of the S protein. The regulatory mechanism aligns
256 with prior studies proposing that fatty acid presence favors the "down" conformation of RBDs[36].
257 The widespread presence of fatty acids in coronaviral S proteins highlights their conserved role
258 in regulating conformational dynamics. Efforts to design small-molecule inhibitors targeting
259 these binding pockets have shown promise but require further structural optimization to
260 enhance efficacy[37].
261 Structural analysis revealed that the HKU5 RBD recognizes ACE2 through a unique
262 mechanism distinct from other ACE2-binding coronaviruses. Unlike the RBM regions of
263 SARS-CoV and SARS-CoV-2, which exhibit conserved ACE2-binding motifs[38], HKU5
264 demonstrates an entirely novel interaction interface. This emphasizes the evolutionary
265 plasticity of coronaviruses, which can utilize the same receptor through diverse binding modes.
266 It also highlights the phenomenon of convergent evolution among unrelated viruses like HKU5,
267 SARS-related viruses, and HCoV-NL63, which all exploit ACE2 as receptor for host cell entry
268 despite limited sequence homology on RBM region of their RBD.
269 The broad tissue expression and high conservation of ACE2 across mammalian species provide
270 a molecular basis for the cross-species transmission of coronaviruses[39,40]. Continuous
271 adaptation of viral S proteins enables optimization of ACE2 binding, as exemplified by the
272 progressive evolution of SARS-CoV-2 variants[41,42]. This interplay between receptor
273 conservation and viral adaptability emphasizes the critical role of ACE2 in shaping coronavirus

host range and transmission potential. For instance, our analysis revealed that certain avian species, such as *Pitta sordida*, possess ACE2 variants capable of binding the HKU5 RBD, suggesting potential zoonotic reservoirs beyond mammals. However, the conclusions drawn from our analysis require further experimental validation. Pseudovirus assays and live virus experiments could be employed to determine whether these ACE2 variants effectively facilitate viral entry and replication.

In summary, our findings advance the understanding of how coronaviruses adapt to diverse hosts via ACE2 utilization, emphasizing the structural and functional diversity of this interaction. By elucidating the roles of fatty acid-mediated conformational regulation and ACE2 as a cross-species receptor, this study highlights the importance of monitoring HKU5 and related viruses for their zoonotic potential and public health implications.

References

1 Fouchier, R. A. *et al.* Aetiology: Koch's postulates fulfilled for SARS virus. *Nature* **423**, 240, doi:10.1038/423240a (2003).

2 Drosten, C. *et al.* Identification of a novel coronavirus in patients with severe acute respiratory syndrome. *N Engl J Med* **348**, 1967-1976, doi:10.1056/NEJMoa030747 (2003).

3 Wu, F. *et al.* A new coronavirus associated with human respiratory disease in China. *Nature* **579**, 265-269, doi:10.1038/s41586-020-2008-3 (2020).

4 Zhou, P. *et al.* A pneumonia outbreak associated with a new coronavirus of probable bat origin. *Nature* **579**, 270-273, doi:10.1038/s41586-020-2012-7 (2020).

5 Ruiz-Aravena, M. *et al.* Ecology, evolution and spillover of coronaviruses from bats. *Nature Reviews Microbiology* **20**, 299-314, doi:10.1038/s41579-021-00652-2 (2022).

6 Mackenzie, J. S., Childs, J. E., Field, H. E., Wang, L. F. & Breed, A. C. *The Role of Bats as Reservoir Hosts of Emerging Neuroviruses*. (Neurotropic Viral Infections. 2016 Apr 8:403-54. doi: 10.1007/978-3-319-33189-8_12.).

7 Letko, M., Seifert, S. N., Olival, K. J., Plowright, R. K. & Munster, V. J. Bat-borne virus diversity, spillover and emergence. *Nature Reviews Microbiology* **18**, 461-471, doi:10.1038/s41579-020-0394-z (2020).

8 Jackson, C. B., Farzan, M., Chen, B. & Choe, H. Mechanisms of SARS-CoV-2 entry into cells. *Nat Rev Mol Cell Biol* **23**, 3-20, doi:10.1038/s41580-021-00418-x (2022).

9 Benton, D. J. *et al.* Receptor binding and priming of the spike protein of SARS-CoV-2 for membrane fusion. *Nature* **588**, 327-330, doi:10.1038/s41586-020-2772-0 (2020).

10 Gui, M. *et al.* Cryo-electron microscopy structures of the SARS-CoV spike glycoprotein reveal a prerequisite conformational state for receptor binding. *Cell Res* **27**, 119-129, doi:10.1038/cr.2016.152 (2017).

11 Wrapp, D. *et al.* Cryo-EM structure of the 2019-nCoV spike in the prefusion conformation. *Science* **367**, 1260-1263, doi:10.1126/science.abb2507 (2020).

12 Ke, Z. *et al.* Structures and distributions of SARS-CoV-2 spike proteins on intact virions. *Nature* **588**, 498-502, doi:10.1038/s41586-020-2665-2 (2020).

13 Nguyen, L. *et al.* Sialic acid-containing glycolipids mediate binding and viral entry of SARS-CoV-2. *Nature Chemical Biology* **18**, 81-90, doi:10.1038/s41589-021-00924-1 (2022).

14 Pronker, M. F. *et al.* Sialoglycan binding triggers spike opening in a human coronavirus. *Nature* **624**, 201-206, doi:10.1038/s41586-023-06599-z (2023).

15 Hulswit, R. J. G. *et al.* Human coronaviruses OC43 and HKU1 bind to 9-O-acetylated sialic acids via a conserved receptor-binding site in spike protein domain A. *Proc Natl Acad Sci U S A* **116**, 2681-2690, doi:10.1073/pnas.1809667116 (2019).

16 Qing, E., Hantak, M., Perlman, S. & Gallagher, T. Distinct Roles for Sialoside and Protein Receptors in Coronavirus Infection. *mBio* **11**, doi:10.1128/mBio.02764-19 (2020).

17 Toelzer, C. *et al.* Free fatty acid binding pocket in the locked structure of SARS-CoV-2 spike protein. *Science* **370**, 725-730, doi:10.1126/science.abd3255 (2020).

18 de Groot, R. J. *et al.* Middle East respiratory syndrome coronavirus (MERS-CoV): announcement of the Coronavirus Study Group. *J Virol* **87**, 7790-7792, doi:10.1128/jvi.01244-13 (2013).

19 Lau, S. K. *et al.* Genetic characterization of Betacoronavirus lineage C viruses in bats reveals marked sequence divergence in the spike protein of pipistrellus bat coronavirus HKU5 in Japanese pipistrelle:

327 implications for the origin of the novel Middle East respiratory syndrome coronavirus. *J Virol* **87**, 8638-
328 8650, doi:10.1128/jvi.01055-13 (2013).
329 20 Woo, P. C., Lau, S. K., Li, K. S., Tsang, A. K. & Yuen, K. Y. Genetic relatedness of the novel human group C
330 betacoronavirus to Tylonycteris bat coronavirus HKU4 and Pipistrellus bat coronavirus HKU5. *Emerg*
331 *Microbes Infect* **1**, e35, doi:10.1038/emi.2012.45 (2012).
332 21 Woo, P. C. Y. *et al.* Molecular diversity of coronaviruses in bats. *Virology* **351**, 180-187,
333 doi:https://doi.org/10.1016/j.virol.2006.02.041 (2006).
334 22 Catanzaro, N. J. *et al.* ACE2 from Pipistrellus abramus bats is a receptor for HKU5
335 coronaviruses. *bioRxiv*, 2024.2003.2013.584892, doi:10.1101/2024.03.13.584892 (2024).
336 23 Li, W. *et al.* Angiotensin-converting enzyme 2 is a functional receptor for the SARS coronavirus. *Nature*
337 **426**, 450-454, doi:10.1038/nature02145 (2003).
338 24 Hoffmann, M. *et al.* SARS-CoV-2 Cell Entry Depends on ACE2 and TMPRSS2 and Is Blocked by a Clinically
339 Proven Protease Inhibitor. *Cell* **181**, 271-280.e278, doi:10.1016/j.cell.2020.02.052 (2020).
340 25 Hofmann, H. *et al.* Human coronavirus NL63 employs the severe acute respiratory syndrome
341 coronavirus receptor for cellular entry. *Proc Natl Acad Sci U S A* **102**, 7988-7993,
342 doi:10.1073/pnas.0409465102 (2005).
343 26 Medina-Enríquez, M. M. *et al.* ACE2: the molecular doorway to SARS-CoV-2. *Cell Biosci* **10**, 148,
344 doi:10.1186/s13578-020-00519-8 (2020).
345 27 Yuan, Y. *et al.* Cryo-EM structures of MERS-CoV and SARS-CoV spike glycoproteins reveal the dynamic
346 receptor binding domains. *Nat Commun* **8**, 15092, doi:10.1038/ncomms15092 (2017).
347 28 Xia, L., Zhang, Y. & Zhou, Q. Structural basis for the recognition of HCoV-HKU1 by human TMPRSS2. *Cell*
348 *Res* **34**, 526-529, doi:10.1038/s41422-024-00958-9 (2024).
349 29 Staufer, O. *et al.* Synthetic virions reveal fatty acid-coupled adaptive immunogenicity of SARS-CoV-2
350 spike glycoprotein. *Nature Communications* **13**, 868, doi:10.1038/s41467-022-28446-x (2022).
351 30 Yan, R. *et al.* Structural basis for the different states of the spike protein of SARS-CoV-2 in complex with
352 ACE2. *Cell Res* **31**, 717-719, doi:10.1038/s41422-021-00490-0 (2021).
353 31 Xiong, Q. *et al.* Close relatives of MERS-CoV in bats use ACE2 as their functional receptors. *Nature* **612**,
354 748-757, doi:10.1038/s41586-022-05513-3 (2022).
355 32 Starr, T. N. *et al.* ACE2 binding is an ancestral and evolvable trait of sarbecoviruses. *Nature* **603**, 913-918,
356 doi:10.1038/s41586-022-04464-z (2022).
357 33 Ma, C. *et al.* Identification of ACE2 as the Entry Receptor for Two Novel European Bat Merbecoviruses.
358 *bioRxiv*, 2023.2010.2002.560486, doi:10.1101/2023.10.02.560486 (2023).
359 34 Chakrabarti, S. *et al.* Touch sensation requires the mechanically gated ion channel ELKIN1. *Science* **383**,
360 992-998, doi:10.1126/science.adl0495 (2024).
361 35 Bangaru, S. *et al.* Structural mapping of antibody landscapes to human betacoronavirus spike proteins.
362 *Sci Adv* **8**, eabn2911, doi:10.1126/sciadv.abn2911 (2022).
363 36 Hills, F. R. *et al.* Variation in structural motifs within SARS-related coronavirus spike proteins. *PLoS*
364 *Pathog* **20**, e1012158, doi:10.1371/journal.ppat.1012158 (2024).
365 37 Wang, Q. *et al.* In Silico Discovery of Small Molecule Modulators Targeting the Achilles' Heel of SARS-
366 CoV-2 Spike Protein. *ACS Cent Sci* **9**, 252-265, doi:10.1021/acscentsci.2c01190 (2023).
367 38 Yan, R. *et al.* Structural basis for the recognition of SARS-CoV-2 by full-length human ACE2. *Science* **367**,
368 1444-1448, doi:10.1126/science.abb2762 (2020).
369 39 Damas, J. *et al.* Broad Host Range of SARS-CoV-2 Predicted by Comparative and Structural Analysis of
370 ACE2 in Vertebrates. *bioRxiv*, doi:10.1101/2020.04.16.045302 (2020).

371 40 Ma, C.-B. *et al.* Multiple independent acquisitions of ACE2 usage in MERS-related coronaviruses. *bioRxiv*,
372 2023.2010.2002.560486, doi:10.1101/2023.10.02.560486 (2024).
373 41 Li, L. *et al.* Structural basis of human ACE2 higher binding affinity to currently circulating Omicron SARS-
374 CoV-2 sub-variants BA.2 and BA.1.1. *Cell* **185**, 2952-2960.e2910, doi:10.1016/j.cell.2022.06.023 (2022).
375 42 Feng, L. *et al.* Structural and molecular basis of the epistasis effect in enhanced affinity between SARS-
376 CoV-2 KP.3 and ACE2. *bioRxiv*, 2024.2009.2003.610799, doi:10.1101/2024.09.03.610799 (2024).
377 43 Zheng, S. Q. *et al.* MotionCor2: anisotropic correction of beam-induced motion for improved cryo-
378 electron microscopy. *Nat Methods* **14**, 331-332, doi:10.1038/nmeth.4193 (2017).
379 44 Grant, T. & Grigorieff, N. Measuring the optimal exposure for single particle cryo-EM using a 2.6 Å
380 reconstruction of rotavirus VP6. *Elife* **4**, e06980, doi:10.7554/eLife.06980 (2015).
381 45 Punjani, A., Rubinstein, J. L., Fleet, D. J. & Brubaker, M. A. cryoSPARC: algorithms for rapid unsupervised
382 cryo-EM structure determination. *Nat Methods* **14**, 290-296, doi:10.1038/nmeth.4169 (2017).
383 46 Rosenthal, P. B. & Henderson, R. Optimal determination of particle orientation, absolute hand, and
384 contrast loss in single-particle electron cryomicroscopy. *J Mol Biol* **333**, 721-745,
385 doi:10.1016/j.jmb.2003.07.013 (2003).
386 47 Chen, S. *et al.* High-resolution noise substitution to measure overfitting and validate resolution in 3D
387 structure determination by single particle electron cryomicroscopy. *Ultramicroscopy* **135**, 24-35,
388 doi:10.1016/j.ultramic.2013.06.004 (2013).
389 48 Abramson, J. *et al.* Accurate structure prediction of biomolecular interactions with AlphaFold 3. *Nature*
390 **630**, 493-500, doi:10.1038/s41586-024-07487-w (2024).
391 49 Trabuco, L. G., Villa, E., Mitra, K., Frank, J. & Schulten, K. Flexible fitting of atomic structures into electron
392 microscopy maps using molecular dynamics. *Structure* **16**, 673-683, doi:10.1016/j.str.2008.03.005
393 (2008).
394 50 Emsley, P., Lohkamp, B., Scott, W. G. & Cowtan, K. Features and development of Coot. *Acta Crystallogr*
395 *D Biol Crystallogr* **66**, 486-501, doi:10.1107/s0907444910007493 (2010).
396 51 Adams, P. D. *et al.* PHENIX: a comprehensive Python-based system for macromolecular structure
397 solution. *Acta Crystallogr D Biol Crystallogr* **66**, 213-221, doi:10.1107/s0907444909052925 (2010).
398 52 Ma, J. *et al.* Cryo-EM structure of S-Trimer, a subunit vaccine candidate for COVID-19. *J Virol* **95**,
399 doi:10.1128/jvi.00194-21 (2021).
400 53 Carrique, L. *et al.* The SARS-CoV-2 Spike harbours a lipid binding pocket which modulates stability of the
401 prefusion trimer. *bioRxiv*, 2020.2008.2013.249177, doi:10.1101/2020.08.13.249177 (2020).
402 54 Tong, L. *et al.* A Retinol Derivative Inhibits SARS-CoV-2 Infection by Interrupting Spike-Mediated Cellular
403 Entry. *mBio* **13**, e0148522, doi:10.1128/mbio.01485-22 (2022).
404 55 Toelzer, C. *et al.* The free fatty acid-binding pocket is a conserved hallmark in pathogenic β-coronavirus
405 spike proteins from SARS-CoV to Omicron. *Sci Adv* **8**, eadc9179, doi:10.1126/sciadv.adc9179 (2022).
406 56 Zhang, S. *et al.* Bat and pangolin coronavirus spike glycoprotein structures provide insights into SARS-
407 CoV-2 evolution. *Nat Commun* **12**, 1607, doi:10.1038/s41467-021-21767-3 (2021).

408

409

410 **Materials and Methods**

411 **Protein preparation**

412 The extracellular domain (ECD) (1~1293 a.a.) of the S protein of BatCoV-HKU5 (uniport ID:
413 A3EXD0) was cloned into the pCAG vector (Invitrogen) with a C-terminal T4 fibritin
414 trimerization motif followed by a Flag tag and a 10×His tag. A "GSAS" mutation at residues
415 742 to 745 was introduced into the S protein to prevent the host cellular protease digestion.
416 Double mutants of the S protein (S_{DM}) were generated with a standard two-step PCR based
417 strategy. The RBD domains of the S protein of different HKU5 lineages, including BatCoV-
418 HKU5 (uniport ID: A3EXD0), BatCoV-HKU5-3 (GenBank: ABN10893.1), BtPa-
419 BetaCoV/GD2013 (GenBank: AIA62343.1) and BatCoV-HKU5-Realted (GenBank:
420 QHA24687.1), were also cloned into the pCAG vector (Invitrogen) with an N-terminal signal
421 peptide for secretion of luciferase and a C-terminal 10×His tag. The PD domains of ACE2 of
422 different species, including *Pipistrellus abramus* (uniport ID: C7ECT9, *Pa*PD, 18~615 a.a.),
423 *Pitta sordida* (uniport ID: A0A851FF99, *Ps*PD, 18~617 a.a.) and *Homo sapiens* (uniport ID:
424 Q9BYF1, *Hs*PD, 25-622 a.a.), were also cloned into the pCAG vector (Invitrogen) with an N-
425 terminal signal peptide for secretion of luciferase followed by an N-terminal 2×StrepII tag and
426 a C-terminal 10×His tag. All the plasmids used to transfect cells were prepared by GoldHi
427 EndoFree Plasmid Maxi Kit (CWBIO). The purification processes of these proteins were same
428 as the S protein of HKU1-B that we have been described previously[28]. Briefly, HEK293F
429 mammalian cells (Invitrogen) were cultured in SMM293-TII medium (Sino Biological) at 37°C
430 and 5% CO_2 in a Multitron-Pro shaker (Infors, 130 rpm). When the cell density reached 2.0×10^6
431 cells/mL, the plasmid was transiently transfected into the cells. To transfect one liter of cell
432 culture, approximately 1.5 mg of plasmid was premixed with 3 mg of polyethylenimine (PEI)

433 (Yeasen Biotechnology) in 50 mL of fresh medium for 30 minutes before being added to the
434 cell culture. After 70 hours of overexpression, cells were removed by centrifugation at 4000×g
435 for 15 minutes. The secreted proteins were purified by Ni-NTA Agarose (GE Healthcare). After
436 loading two times, the Ni-NTA Agarose was washed with the wash buffer containing 25 mM
437 Tris (pH 8.0), 150 mM NaCl, 50 mM imidazole. The protein was eluted with the elute buffer
438 containing 25 mM Tris (pH 8.0), 150 mM NaCl, 500 mM imidazole. The eluent of RBDs or
439 PDs was concentrated and subject to size-exclusion chromatography (SEC, Superdex 200
440 Increase 10/300 GL, GE Healthcare) in buffer containing 25 mM Tris (pH 8.0), 150 mM NaCl.
441 The eluent of S or S_{DM} protein was subject to SEC (Superose 6 Increase 10/300 GL, GE
442 Healthcare) in buffer containing 25 mM Tris (pH 8.0), 150 mM NaCl. The HKU5 RBD was
443 incubated with *Pa*PD or *Ps*PD at a molar ratio of about 1:5 for one hour. Then the mixtures
444 were subject to SEC (Superose 6 Increase 10/300 GL, GE Healthcare) in buffer containing 25
445 mM Tris (pH 8.0), 150 mM NaCl. The peak fractions of SEC were collected and concentrated
446 for cryo-EM analysis.
447

448 **Cryo-EM sample preparation and data acquisition**

449 The protein samples were concentrated to ~2.5 mg/mL and applied to the grids. Aliquots (3.5
450 μL) of the protein were placed on glow-discharged holey carbon grids (Quantifoil Au R1.2/1.3).
451 The grids were blotted for 3.5 s and flash-frozen in liquid ethane cooled by liquid nitrogen with
452 Vitrobot (Mark IV, Thermo Scientific). The prepared grids were transferred to a Krios (Thermo
453 Scientific) operating at 300 kV equipped with a Gatan K3 detector and GIF Quantum energy
454 filter. Movie stacks were automatically collected using EPU software (Thermo Scientific), with

455 a slit width of 20 eV on the energy filter and a defocus range from -1.2 μm to -2.2 μm in super-
456 resolution mode at a nominal magnification of 81,000×. Each stack was exposed for 2.56 s with
457 an exposure time of 0.08 s per frame, resulting in a total of 32 frames per stack. The total dose
458 rate was ~50 $e^-/Å^2$ for each stack.
459

460 **Data processing**

461 The movie stacks were motion corrected with MotionCor2[43] and binned two fold, resulting in
462 a pixel size of 1.087 Å/pixel. Meanwhile, dose weighting was performed[44]. After patch CTF
463 estimation, particles were automatically picked according to the templates generated from an
464 initial 2D classification of manually picked particles by cryoSPARC[45]. After 2D classification,
465 the particles with clear features were selected and subject to *ab-initio* reconstruction to obtain
466 the initial models, then multi-hetero refinement without symmetry were performed to selected
467 good particles using cryoSPARC[45]. The selected particles were subject to non-uniform
468 refinement, local CTF refinement or global CTF refinement, and local refinement, resulting in
469 3D reconstruction for the whole structures. The resolution was estimated with the gold-standard
470 Fourier shell correlation 0.143 criterion[46] with high-resolution noise substitution[47].
471

472 **Model building and structure refinement**

473 For the model building, the predicted atomic models by Alphafold 3[48] were used as templates,
474 which were molecular dynamics flexible fitted[49] into the whole cryo-EM maps and manually
475 adjusted with Coot[50] to obtain the atomic models. Each residue was manually checked with the
476 chemical properties taken into consideration during model building. Several segments, whose

477 corresponding densities were invisible, were not modeled. Structural refinement was
478 performed in Phenix[51] with secondary structure and geometry restraints to prevent overfitting.
479

480 **Bio-layer interferometry (BLI)**

481 BLI experiments were performed using the Octet system (ForteBio) to characterize the protein
482 interactions. StrepII-10×His-tagged *Pa*PD and *Ps*PD proteins, along with 10×His-RBD
483 proteins from four HKU5 strains, were purified separately. At room temperature, *Pa*PD
484 proteins were immobilized onto equilibrated streptavidin (SA) biosensors. Subsequently, the
485 biosensors were exposed to solution containing various concentration of RBD proteins (0 nM,
486 12.5 nM, 25 nM, 50 nM, 100 nM, 200 nM, 400 nM, and 800 nM), with binding kinetics
487 monitored in real-time. Following the association phase, the biosensors were immersed in a
488 regeneration buffer to monitor dissociation kinetics in real-time. Sensorgrams were analyzed
489 using Octet data analysis software to determine the binding affinity constants between the PD
490 and RBD proteins. This process was repeated to evaluate the binding affinities between the two
491 PD proteins and the four RBD proteins. For the binding affinity measurements between *Ps*PD
492 and different RBDs, the RBD concentration gradient was set at 0 μM, 0.04 μM, 0.08 μM, 0.16
493 μM, 0.32 μM, 0.64 μM, 1.28 μM, and 2.56 μM.
494

495 **Tripartite split-fluorescence system**

496 We designed a tripartite split-fluorescence system containing plasmid A, B, and C. Plasmid A
497 encoded the first nine β-strands (1~196 a.a.) of sfGFP, followed by a stop codon and an internal
498 ribosome entry site 2 (iRES2) sequence to mediate the subsequent translation of iRFP702. For

499 plasmid B, the tenth β-strand of sfGFP (197~216 a.a.) was inserted at the N-terminus and fused
500 to a receptor-binding domain via a linker
501 (DVGGGGSEGGGSGGPGSGGEGSAGGGSAGGGS). An iRES2 sequence and mCherry
502 sequence were then inserted downstream. For plasmid C, the receptor-binding domain was
503 inserted at the N-terminus and fused to the eleventh β-strand of sfGFP (217~238 a.a.) via a
504 linker (GSGAGGSPGGGSGGSGSSASGGSTSGGGSGGGS), followed by iRES2 and EBFP2
505 sequences. The designed sequences were synthesized by SynbioB and cloned into the
506 mammalian expression vector PCAG.

507 **Flow cytometry sorting and statistical analysis**

508 HEK293F cells were cultured in SMM293-TII medium (Sino Biological) at 37°C with 5% CO_2
509 under shaking conditions (120 rpm). Plasmid A, plasmid B expressing WT or mutant RBD,
510 and plasmid C expressing WT or mutant PD were mixed at a 1:1:1 ratio (5 μg each) and
511 transfected into cells (2×10^6 cells per 5 mL flask) using PEI (Lablead) at a 2:1 DNA-to-PEI
512 mass ratio. After 48 hours, cells were harvested by centrifugation at 200 g for 2 minutes and
513 washed twice with 2 mL PBS (Sangon Biotec) at room temperature. The final cell pellet was
514 resuspended in 1ml PBS for flow cytometry. Flow cytometry was performed on a BD
515 FACSymphony™ A3. Single-cell populations were gated based on forward scatter area (FSC-
516 A), side scatter area (SSC-A), and forward scatter height (FSC-H) parameters. Cells co-
517 expressing plasmids A, B, and C, identified by simultaneous positivity in the BV421 (405 nm
518 laser, 450/50 nm filter), BV711 (405 nm laser, 710/50 nm filter), and PE-CF594 (561 nm laser,
519 610/20 nm filter) fluorescence channels, were analyzed for sfGFP fluorescence intensity in the

FITC channel (488 nm laser, 530/30 nm filter). The median fluorescence intensity of the gated population was calculated using FlowJo v10. All experiments were performed in triplicate.

Data availability

Atomic coordinates and cryo-EM maps (PDB: 9KR8, 9KR9, 9KRA, 9KRB; EMD-62522, EMD-62523, EMD-62524, EMD-62525) have been deposited to the Protein Data Bank (http://www.rcsb.org) and the Electron Microscopy Data Bank (https://www.ebi.ac.uk/pdbe/emdb/), respectively. Correspondence and requests for materials should be addressed to Q.Z. (zhouqiang@westlake.edu.cn)

Acknowledgements

This work is supported by National Natural Science Foundation of China (82241081). We thank the cryo-EM facility, the high-performance computing center, the mass spectrometry and metabolomics core facility, the flow cytometry core facility, the protein characterization and crystallography facility of Westlake University for technical assistance, advice and support.

Author contributions

Q.Z. and L.X. conceived the project. L.X., Y. L., D.L. and Y.Z. did the experiments. L.X. and Y.Z. analyzed the PDB structures and performed the visualization. All authors contributed to the data analysis. Q.Z., L.X. and Y.Z. wrote the manuscript. Q.Z. supervised the project.

Competing interests

The authors declare no competing interests.

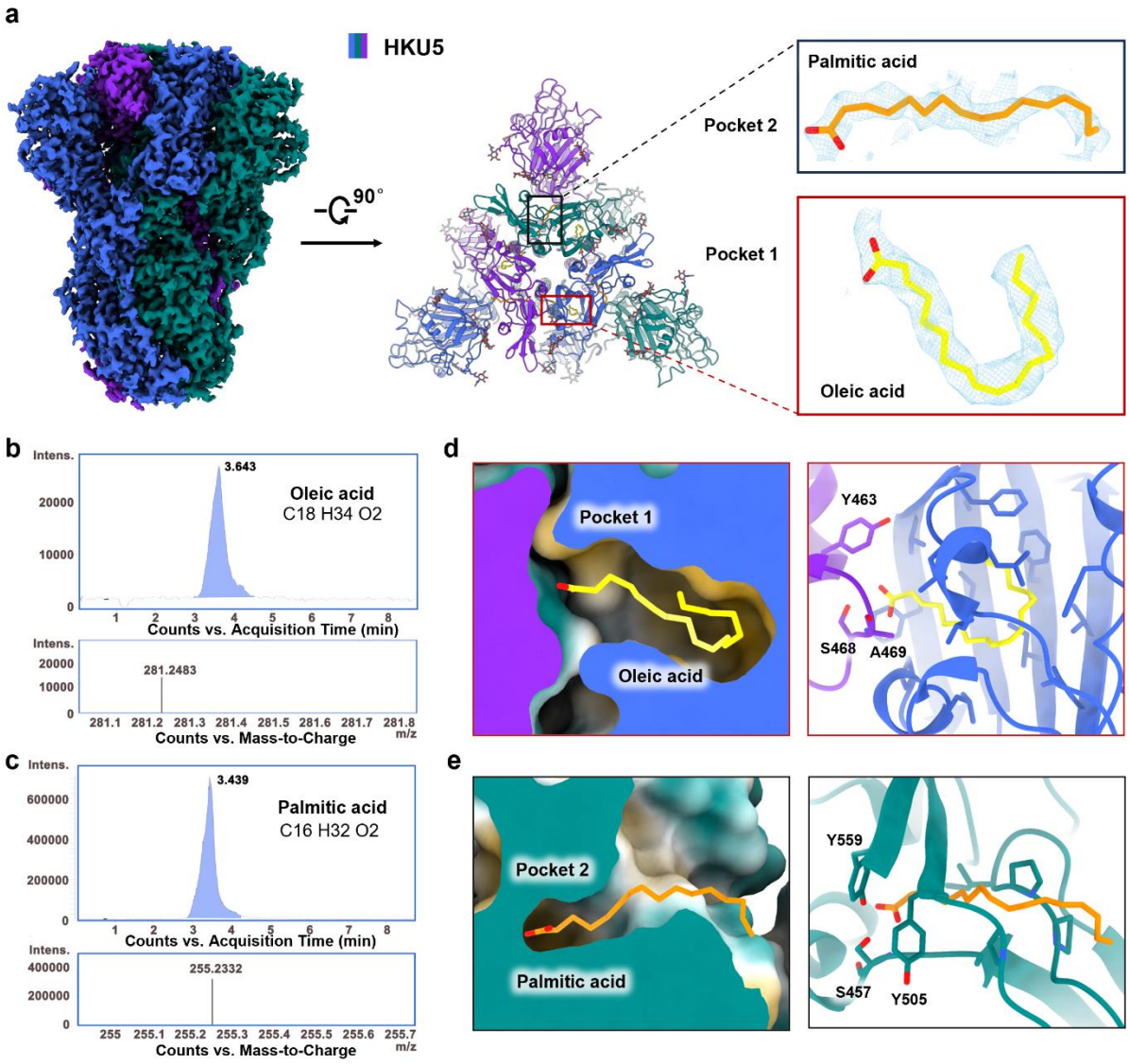

542

543 **Figure 1. Cryo-EM structure of the HKU5 S protein.**

544 (a) The cryo-EM map shown in side view (Left) and the atomic model shown in top view
545 (Middle) of the HKU5 S protein, with protomers displayed in marine blue, purple, and forest
546 green, respectively. Enlarged views of the boxed regions in the middle panel, showing the
547 bound fatty acids (Right), with cryo-EM map shown at threshold of 3 σ for palmitic acid and 4
548 σ for oleic acid, respectively. (b, c) Liquid chromatography-mass spectrometry (LC-MS)
549 analysis of purified HKU5 S protein. (Top) Chromatograms of C18 and C16 fatty acids.
550 (Bottom) Corresponding electrospray ionization time-of-flight (ESI-TOF) mass spectra, with

551 molecular weights of C18H32O2 and C16H34O2 labeled. Intens., i ratio. (d, e) Binding
552 pockets of oleic acid (d) and palmitic acid (e) within the HKU5 S protein, showing key residues
553 involved in polar interactions.
554

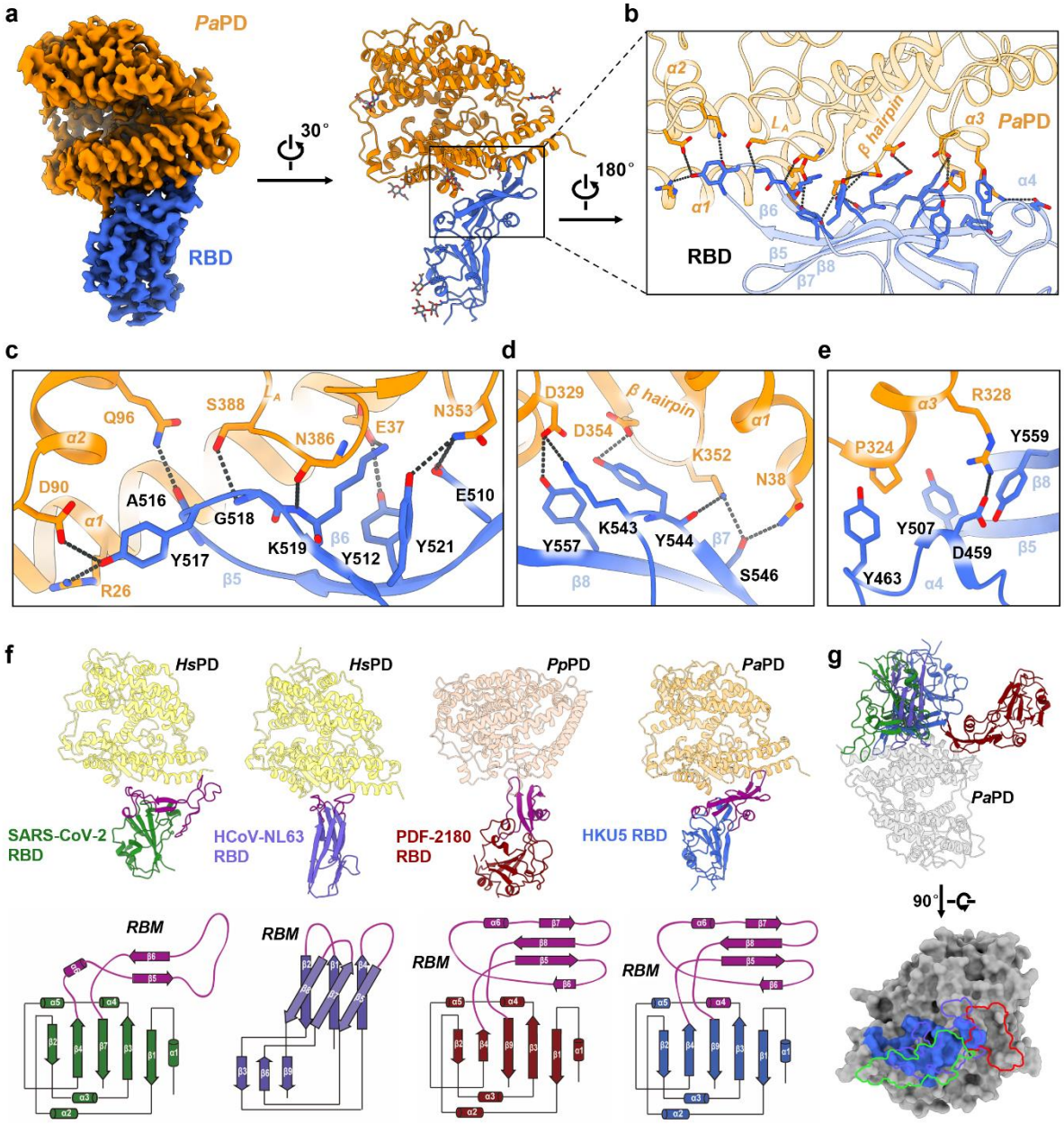

Figure 2. Interactions between HKU5 RBD and bat ACE2.

(a) Cryo-EM map (left) and atomic model shown in cartoon (right) of HKU5 RBD (marine blue) in complex with *Pa*PD (orange). (b) Enlarged view of the interaction interface, showing *Pa*PD α1, α2, α3 helices, β-hairpin, and L_A loop interacting with β-strands 5~8 and the α4 of HKU5 RBD. (c-e) Detailed analysis of the binding interface between HKU5 RBD and *Pa*PD, with polar interactions indicated by dashed black lines. (f) ACE2 binding modes for SARS-

562 CoV-2, HCoV-NL63, PDF-2180, and HKU5 (upper panel), with RBD topologies shown in
563 lower panel and the RBM region marked in purple. *Hs*PD, *Pp*PD, and *Pa*PD are the peptidase
564 domains of *Homo sapiens*, *Pipistrellus pipistrellus*, and *Pipistrellus abramus*, respectively. (g)
565 Superimposed ACE2 binding sites of SARS-CoV-2, HCoV-NL63, PDF-2180, and HKU5 on
566 *Pa*PD (upper panel). Binding footprints (lower panel) are shown in green (SARS-CoV-2),
567 violet (HCoV-NL63), red (PDF-2180) and marine blue (HKU5), respectively, emphasizing the
568 unique HKU5 binding epitope.
569

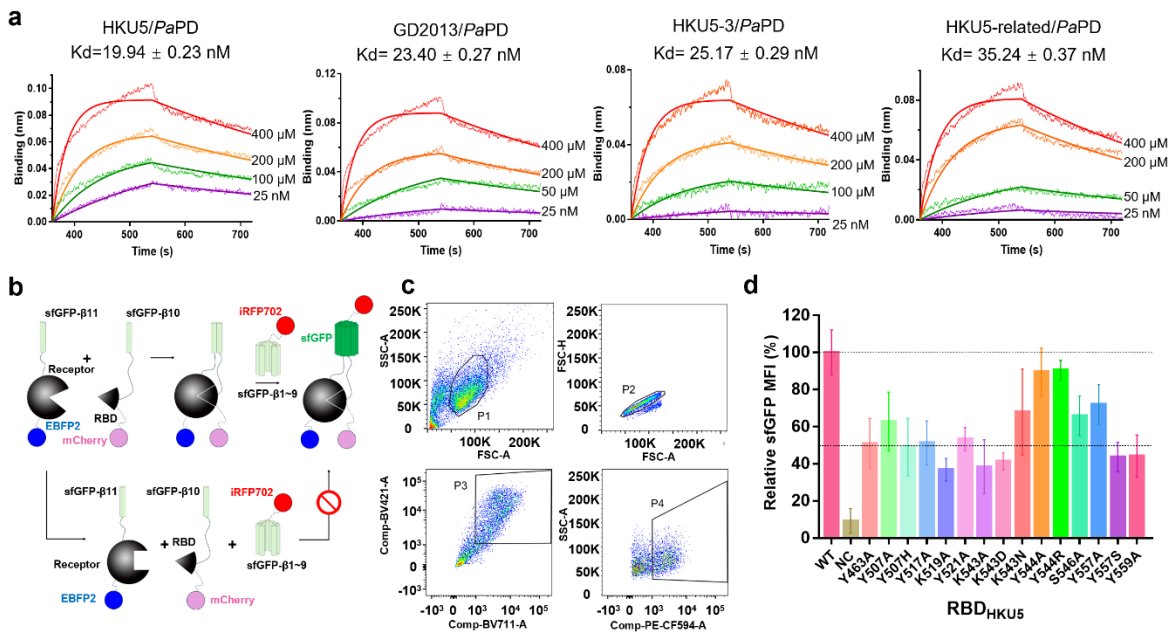

Figure 3. Interaction and functional analysis of HKU5 lineage RBDs with *Pa*PD.

(a) Binding and dissociation kinetics of RBDs of four HKU5 lineages (A3EXD0, AIA62343.1, ABN10893.1, and QHA24687.1) with *Pa*PD measured by biolayer interferometry (BLI). R^2 values are 0.9776, 0.9830, 0.9867, and 0.9861, respectively. (b) Experimental schematic of tripartite split-fluorescence system to evaluate HKU5 RBD-*Pa*PD interactions. (c) Flow cytometry-based sorting of single-cell populations expressing HKU5 RBD and *Pa*PD. Populations P2 and P4 were isolated based on fluorescence gating. And sfGFP fluorescence intensity in the P4 population was measured. (d) Relative sfGFP fluorescence intensity for WT or mutant HKU5 RBDs binding *Pa*PD, normalized to the WT signal. Each data represents mean ± standard deviation of three separate measurements.

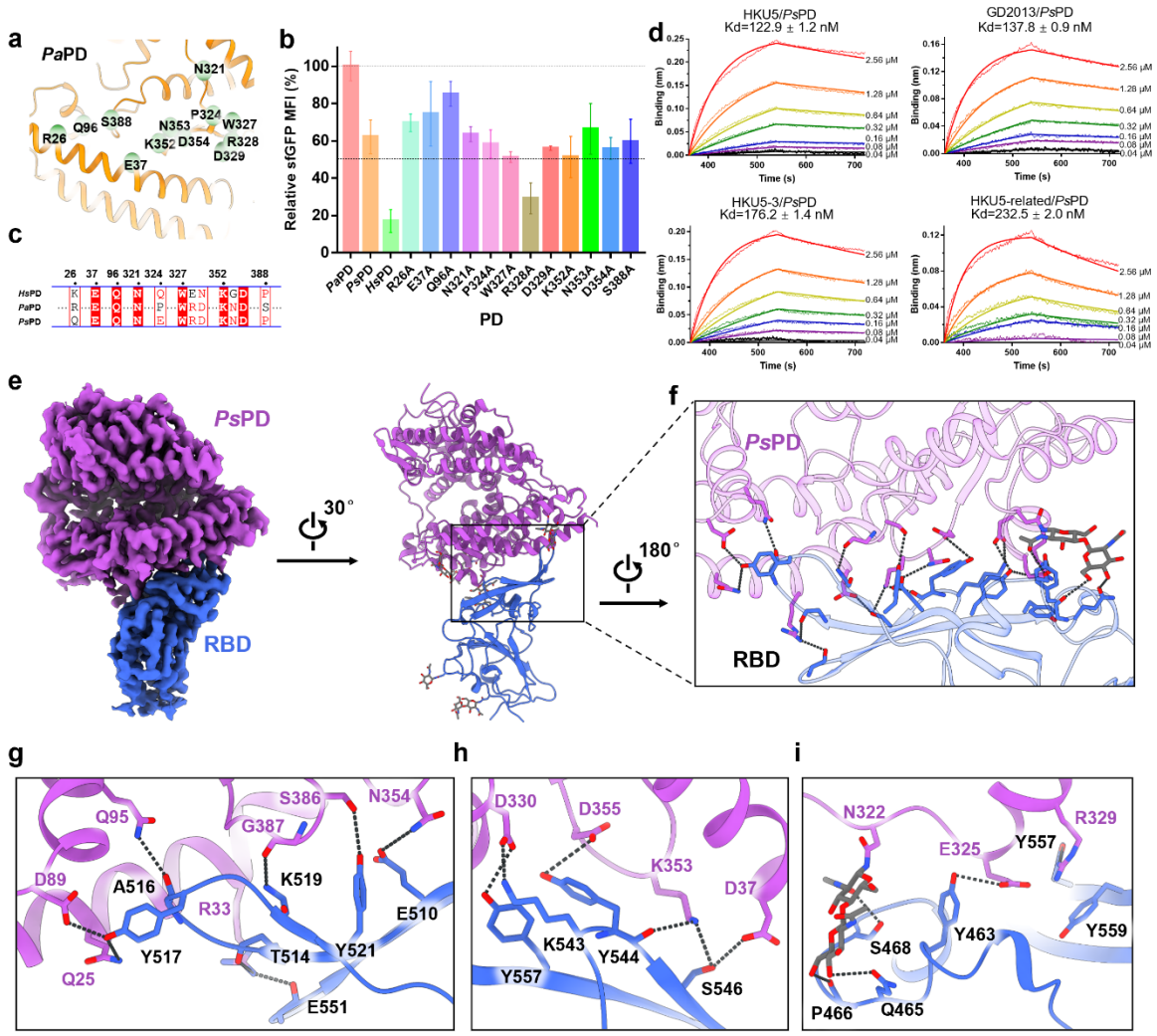

Figure 4. Mutational analysis of ACE2 interface residues and cross-species RBD interactions. (a) Critical interface residues of *Pa*PD involved in HKU5 RBD binding. (b) Effects of *Pa*PD residue mutations on HKU5 RBD binding, evaluated by flow cytometry and tripartite split-fluorescence-based assays. The sfGFP fluorescence intensity was normalized to WT *Pa*PD. (c) Conservation analysis of *Pa*PD interface residues in humans and red-whiskered bulbuls, highlighting conserved residues essential for cross-species interactions. (d) Binding affinities of RBDs of four HKU5 lineages (A3EXD0, AIA62343.1, ABN10893.1, and QHA24687.1) with bulbul ACE2 PD (*Ps*PD), determined using BLI. R^2 values are 0.9963, 0.9973, 0.9956, and 0.9892, respectively. (e) Cryo-EM map (left panel) and structural model

592 (right panel) of HKU5 RBD (marine blue) in complex with *Ps*PD (purple), showing critical
593 binding interactions. (f-i) Detailed analysis of interface interactions between *Ps*PD and HKU5
594 RBD, with polar interactions indicated by dashed black lines.

595

596

597

598

599

600

601

602

603

604

605

606

607

608

609

610

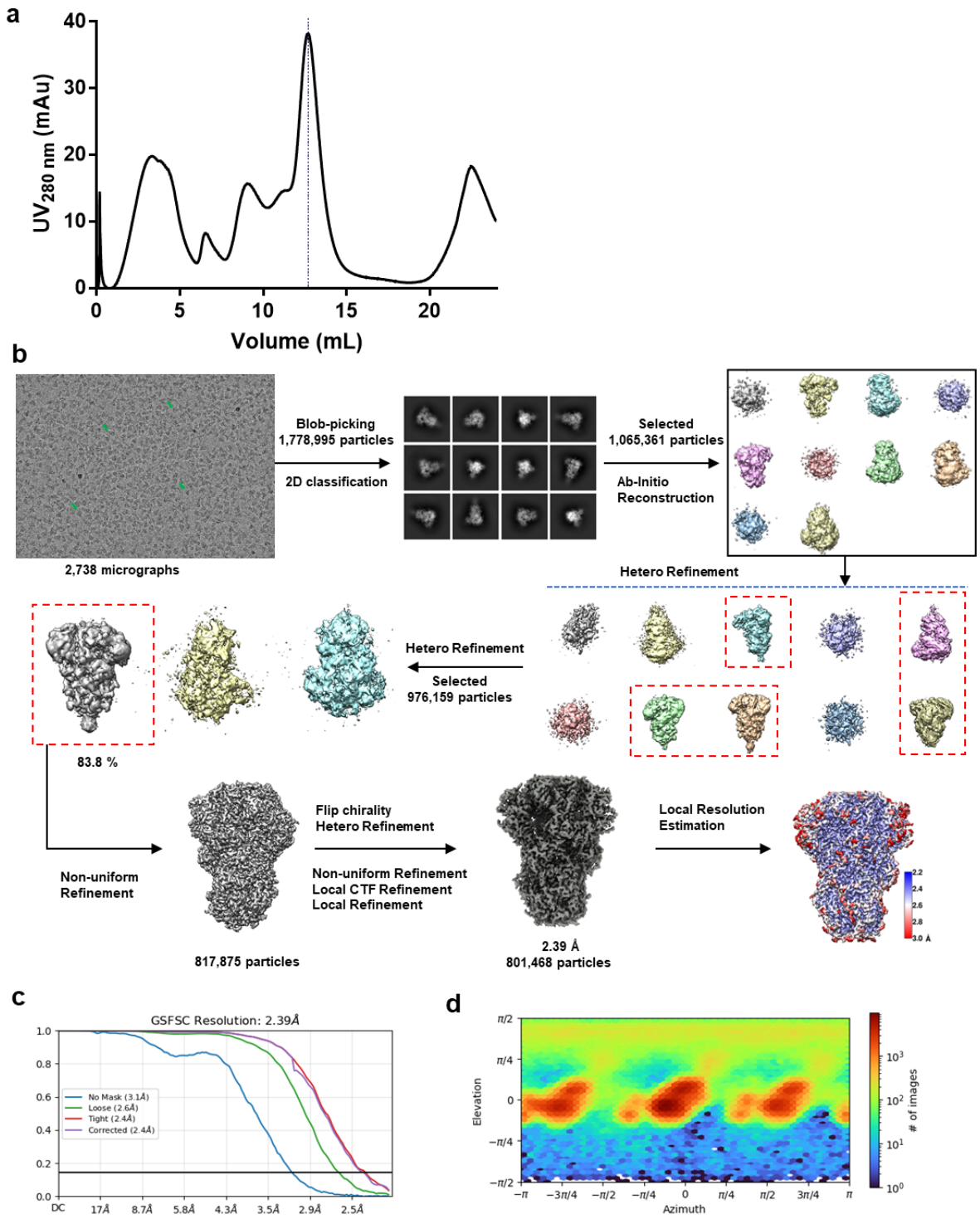

Supplementary information, Figure S1. Cryo-EM data processing pipeline and analysis for the HKU5 S protein.

(a) Gel filtration elution profile of HKU5 S protein. (b) Flowchart of Cryo-EM data processing, please see the "Data Processing" section in Materials and Methods for details. (c)

616 Gold standard FSC curve of the HKU5 S protein is estimated by cryoSPARC. (d) Euler angle

617 distribution of the HKU5 S protein in the final 3D reconstruction in cryoSPARC.

618

a

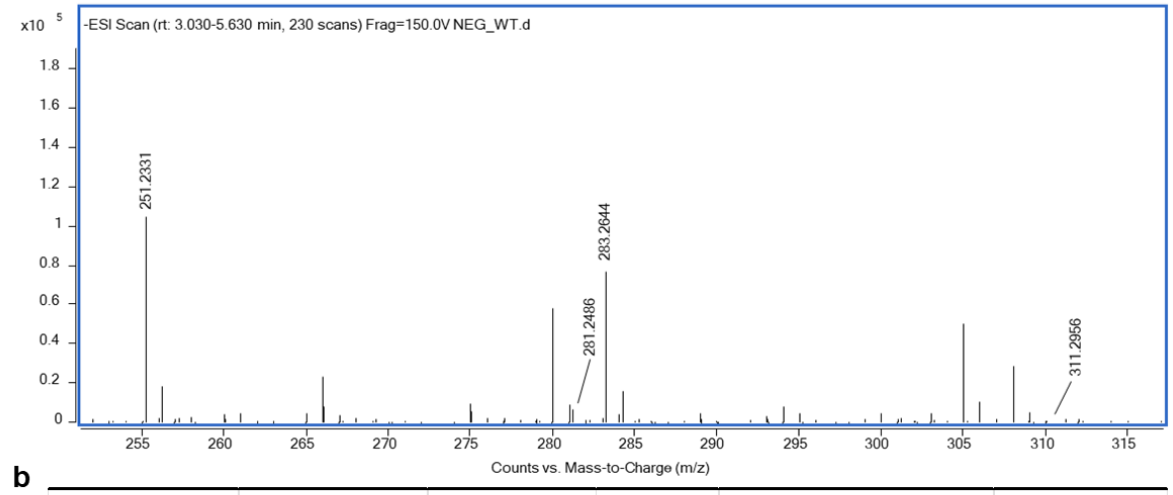

b

Compound Name	Formula	Mass	RT	NEG_WT (Area)	SNR
FA 18:0	C18 H36 O2	284.2716	4.37	11196418.18	252.2
FA 16:0	C16 H32 O2	256.2404	3.44	15968231.22	15874.9
FA 18:1	C18 H34 O2	282.2556	3.64	674911.7934	6176.9
FA 20:0	C20 H40 O2	312.3026	5.19	215788.3878	18.3

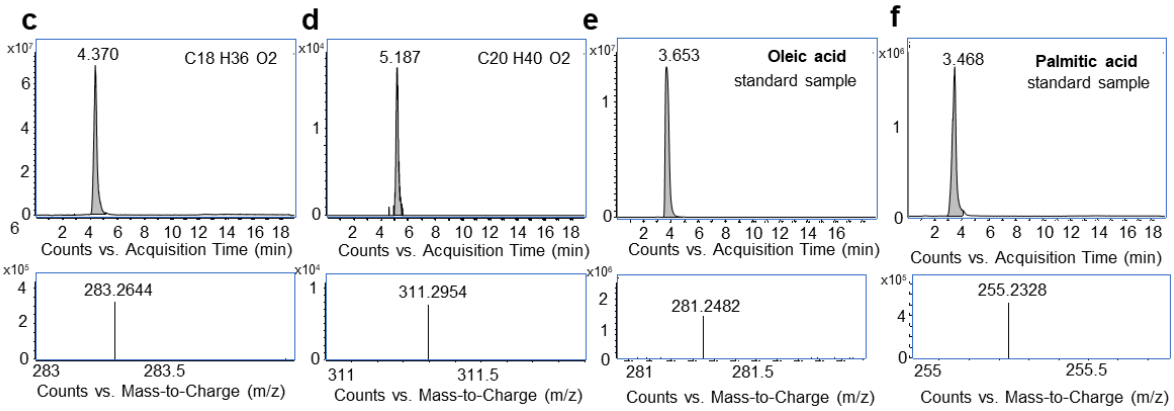

Supplementary information, Figure S2. Mass spectrometry characterization of the HKU5 S protein.

(a) The mass spectrometry profile of the HKU5 S protein. The x-axis represents the m/z ratio, which is the mass-to-charge ratio of the ions. The y-axis represents the ion intensity, reflecting the abundance of the ions in the sample. Each peak in the mass spectrum corresponds to a specific ion. (b) The information of the identified compounds. RT: retention time, NEG_WT: negative ion peak area, SNR: signal-to-noise ratio. The NEG_WT is proportional to the

627 compound concentration. (c) and (d) are the mass spectra of octadecanoic acid (FA 18:0) and
628 eicosanoic acid (FA 20:0), respectively. (e) and (f) display the standard mass spectra of oleic
629 acid and palmitic acid, respectively. These standard spectra serve as references for the
630 qualitative identification of compounds in the sample.
631

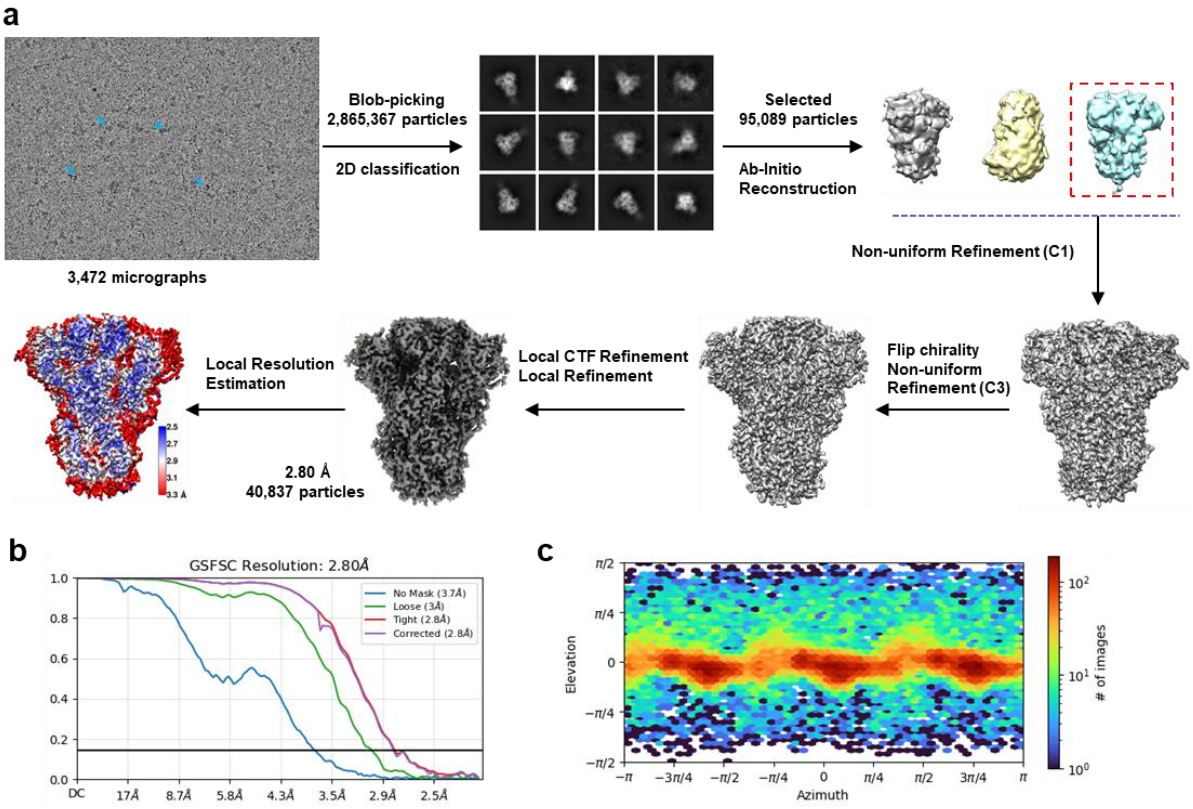

Supplementary information, Figure S3. Cryo-EM data processing pipeline and analysis for the HKU5 S_{DM} protein.

(a) Flowchart of Cryo-EM data processing, please see the "Data Processing" section in Materials and Methodsfor details. (b) Gold standard FSC curve of the HKU5 S_{DM} protein is estimated by cryoSPARC. (c) Euler angle distribution of the HKU5 S_{DM} protein in the final 3D reconstruction in cryoSPARC.

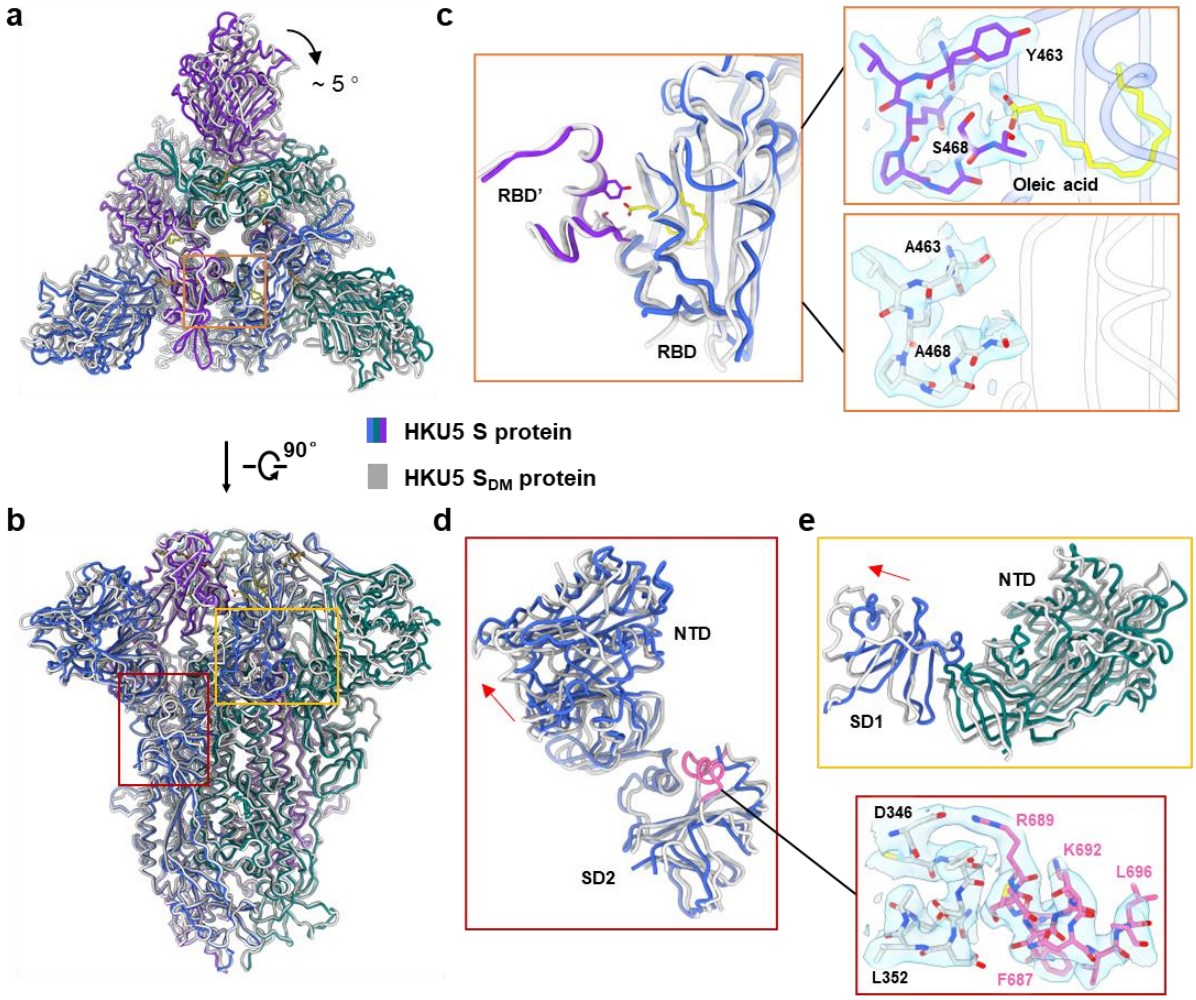

Supplementary information, Figure S4. Structural comparison of the WT HKU5 S protein and the S_{DM} protein.

(a) and (b) show the overall structural comparison between the WT HKU5 S protein and the S_{DM} protein, viewed from two orthogonal orientations. (c) The comparison of the local structure and the cryo-EM map of the WT HKU5 S protein and the S_{DM} protein at the oleic acid binding site. The oleic acid molecule is shown in yellow, and the residues are represented as stick models. The results show that the mutations cause significant changes in the local structure, eliminating the binding of the oleic acid molecule. (d) and (e) show the local structural changes in the NTD of the HKU5 S protein upon oleic acid binding. Red arrows indicate the direction

651 of structural movement, and pink regions represent the remodeled secondary structures in the

652 HKU5 S_{DM} protein.

653

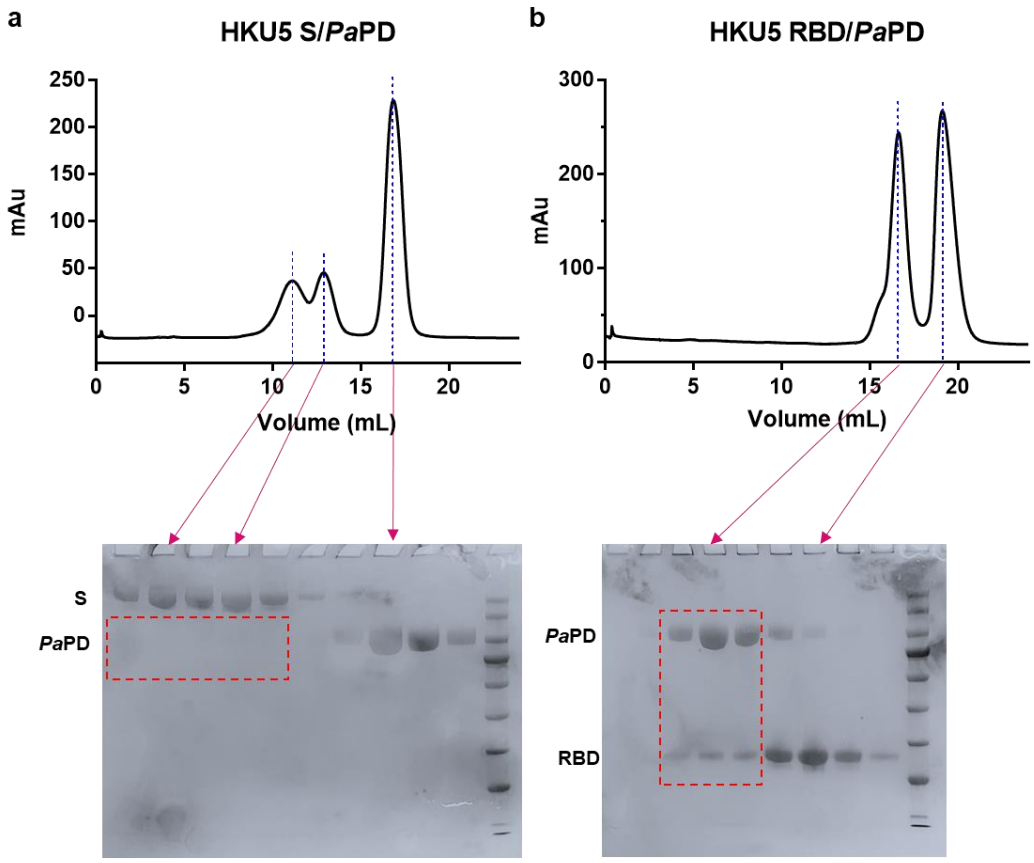

Supplementary information, Figure S5. Gel filtration and SDS-PAGE analysis of the HKU5 S protein or its RBD incubated with *Pa*PD.

(a) Top: Gel filtration elution profile of HKU5 S protein and *Pa*PD incubated at a molar ratio of 1:5 for 1 hour. Bottom: SDS-PAGE analysis of fractions collected from the gel filtration. The results indicate that HKU5 S protein and *Pa*PD do not co-elute, suggesting that they do not form a stable complex under these conditions. (b) Top: Gel filtration elution profile of HKU5 RBD and *Pa*PD incubated at a molar ratio of 1:5 for 1 hour. Bottom: SDS-PAGE analysis of fractions collected from the gel filtration. The results indicate that HKU5 RBD and *Pa*PD can be co-eluted, suggesting that they form a stable complex under these conditions.

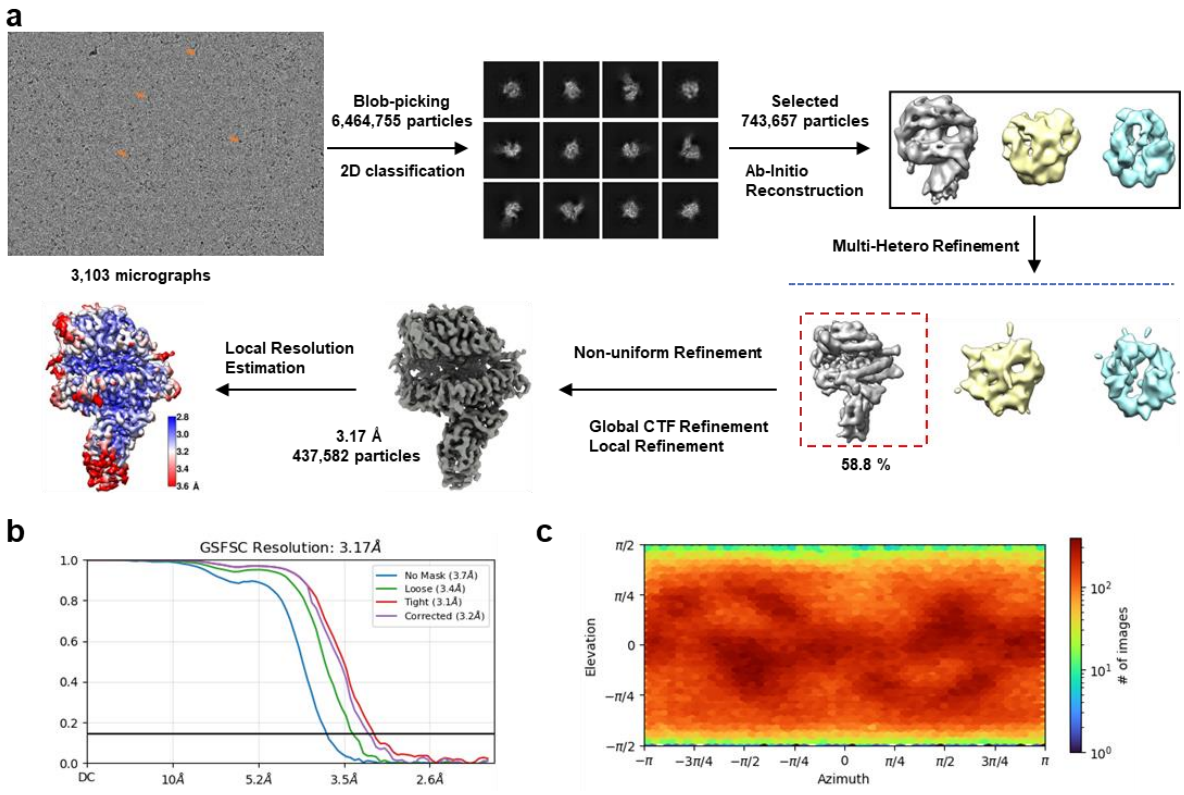

Supplementary information, Figure S6. Cryo-EM data processing pipeline and analysis for the HKU5 RBD–*Pa*PD complex.

(a) Flowchart of Cryo-EM data processing, please see the "Data Processing" section in Materials and Methods for details. (b) Gold standard FSC curve of the HKU5 RBD–*Pa*PD complex is estimated by cryoSPARC. (c) Euler angle distribution of the HKU5 RBD–*Pa*PD complex in the final 3D reconstruction in cryoSPARC.

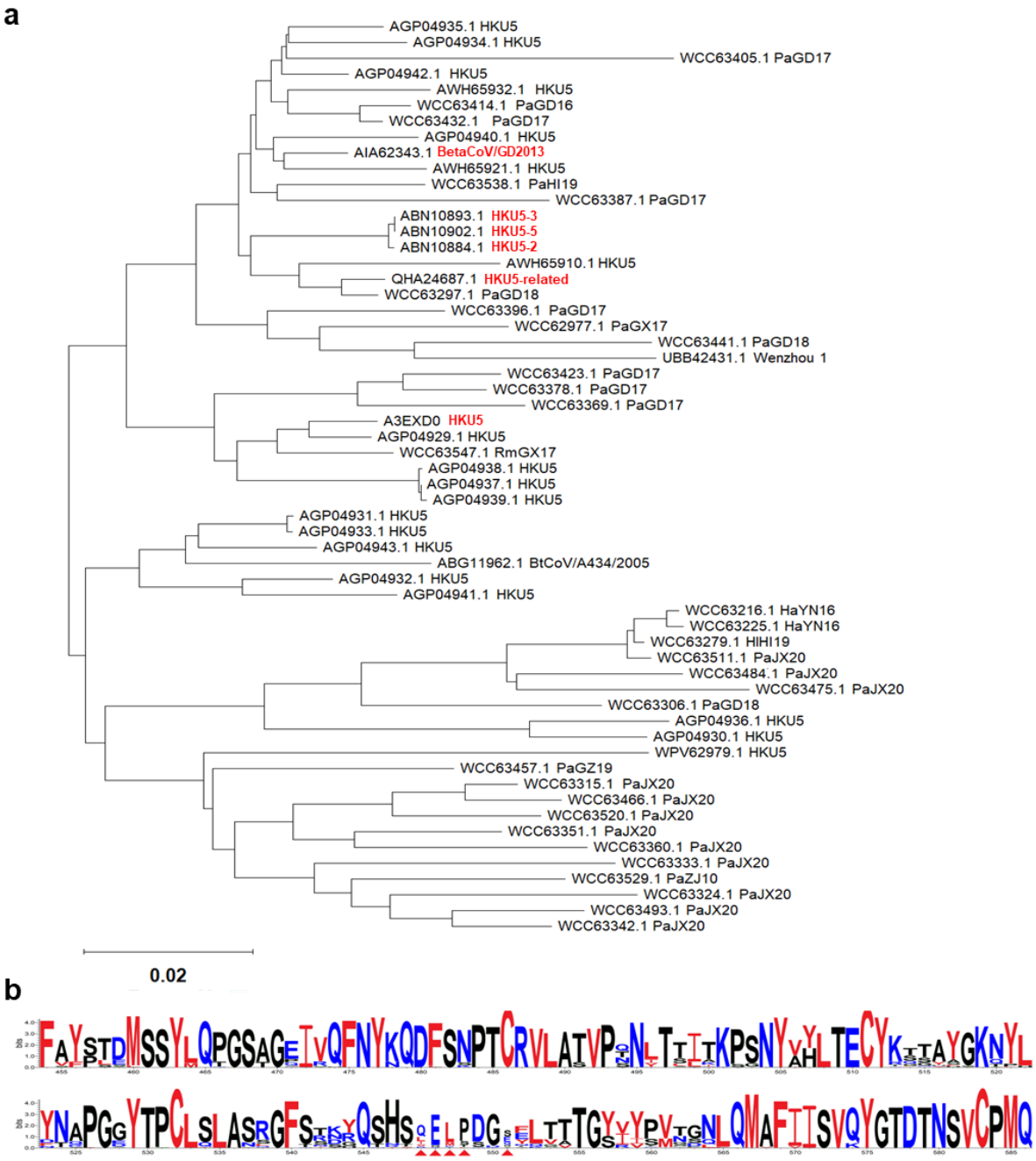

Supplementary information, Figure S7. Phylogenetic analysis and sequence conservation logo of the RBM region of HKU5 lineages.

(a) Phylogenetic tree of the S protein sequences in the NCBI protein database with >80% identity to the HKU5 S protein. (b) The sequence conservation logo with conserved interface residues highlighted. The insertion mutations are marked by solid red triangles. The viruse and protein accession numbers are as follows: Pipistrellus bat coronavirus HKU5 (A3EXD0,

AGP04929.1, AGP04937.1, AGP04939.1, AGP04938.1, AGP04942.1, AGP04935.1, AGP04934.1, AGP04940.1, AGP04932.1, AWH65921.1, AGP04931.1, AGP04933.1, AGP04936.1, AGP04943.1, AGP04930.1), BtPa_BetaCoV/GD2013 (AIA62343.1), HKU5-2 (ABN10884.1), HKU5-3 (ABN10893.1), HKU5-related (QHA24687.1), HKU5-5 (ABN10902.1), Bat Coronavirus RmGX17 (WCC63547.1), Bat Coronavirus PaHI19 (WCC63538.1), Bat Coronavirus PaGZ19 (WCC63457.1), Bat Coronavirus PaJX20 (WCC63315.1, WCC63520.1, WCC63529.1), Bat Coronavirus PaGD16 (WCC63315.1, WCC63520.1, WCC63529.1), Bat Coronavirus PaGD17 (WCC63423.1, WCC63378.1, WCC63369.1, WCC63396.1, WCC63414.1, WCC63432.1, WCC63387.1, WCC63351.1, WCC63441.1), and Bat Coronavirus PaGD18 (WCC63297.1, WCC63396.1).

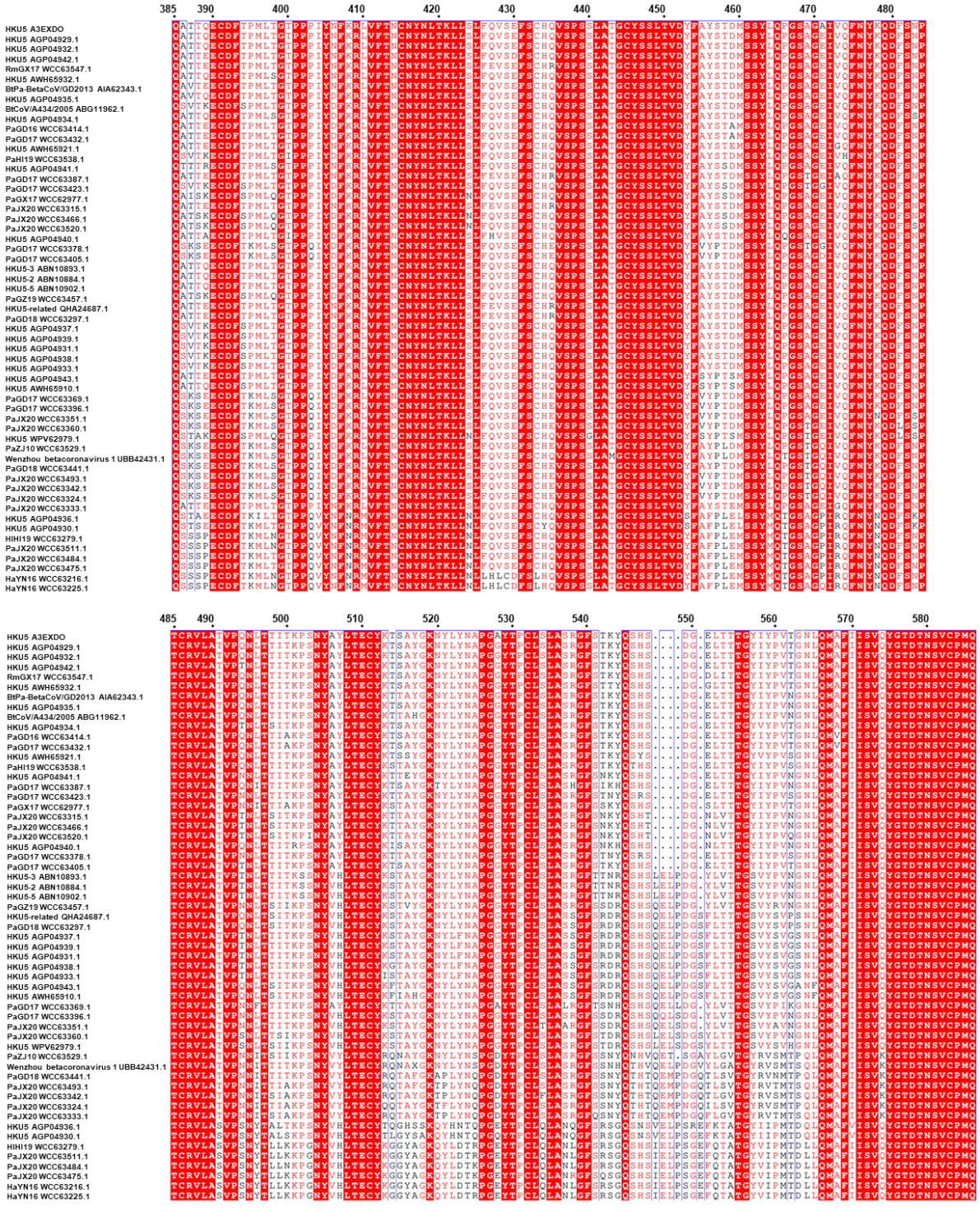

Supplementary information, Figure S8. Multiple sequence alignment of RBD from different HKU5 subtypes.

694 The specific viruses and their corresponding protein accession numbers are detailed in
695 Supplementary information, Fig. S7

696

697

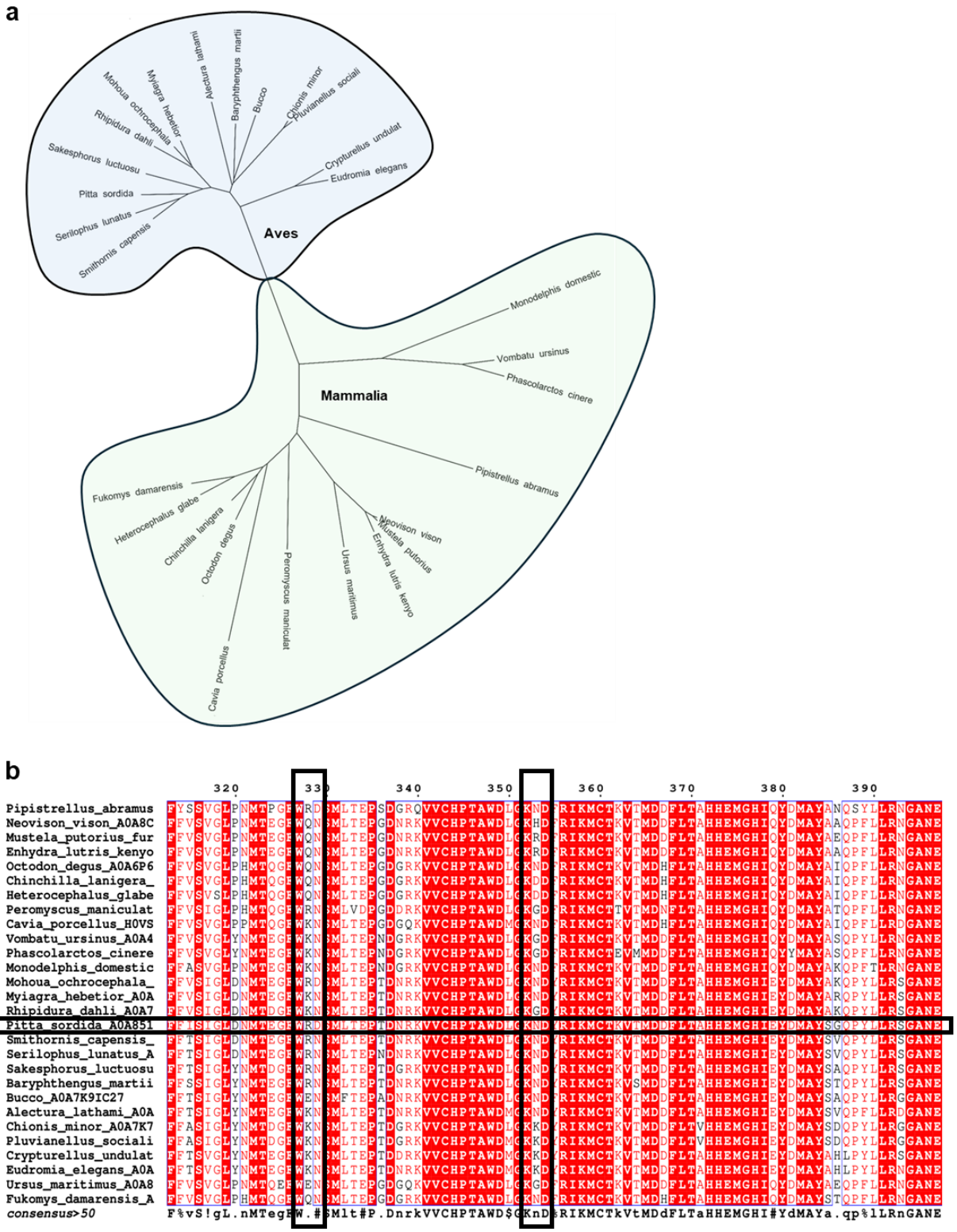

Supplementary information, Figure S9. Evolutionary analysis of *Pipistrellus abramus* ACE2 homologous sequences.

701 (a) Phylogenetic tree of *Pipistrellus abramus* ACE2 homologous sequences. Avian species are
702 marked in light blue, and mammalian species are marked in light green. (b) Multiple sequence
703 alignment of ACE2 homologous sequences from multiple species. The conserved motifs are
704 indicated by black boxes. The species and protein accession numbers are as follows:
705 *Pipistrellus abramus* (C7ECT9), *Neovison vison* (A0A8C7BTF2), *Octodon degus*
706 (A0A6P6ESQ8), *Enhydra lutris kenyoni* (A0A2Y9KLV0), *Mustela putorius furo* (Q2WG88),
707 *Heterocephalus glaber* (G5C234), *Chinchilla lanigera* (A0A8C2UPB0), *Peromyscus*
708 *maniculatus bairdii* (A0A6I9KY05), *Vombatus ursinus* (A0A4X2M679), *Monodelphis*
709 *domestica* (F6WXR7), *Phascolarctos cinereus* (A0A6P5M0G0), *Ursus maritimus*
710 (A0A8M1G354), *Fukomys damarensis* (A0A091D044), *Mohoua ochrocephala*
711 (A0A7K7XXX4), *Pitta sordida* (A0A851FF99), *Smithornis capensis* (A0A7K8QUJ4),
712 *Myiagra hebetior* (A0A7K9J5U7), *Serilophus lunatus* (A0A7L1DC41), *Rhipidura dahli*
713 (A0A7K9W0V6), *Sakesphorus luctuosus* (A0A7K8YCL7), *Crypturellus undulatus*
714 (A0A7K4LNH7), *Chionis minor* (A0A7K7FWK2), *Baryphthengus martii* (A0A7K9DU94),
715 *Alectura lathami* (A0A7L0W6I4), *Pluvianellus socialis* (A0A7L3D992), *Bucco*
716 (A0A7K9IC27), *Eudromia elegans* (A0A7K7VCA6), *Cavia porcellus* (H0VSF6).
717

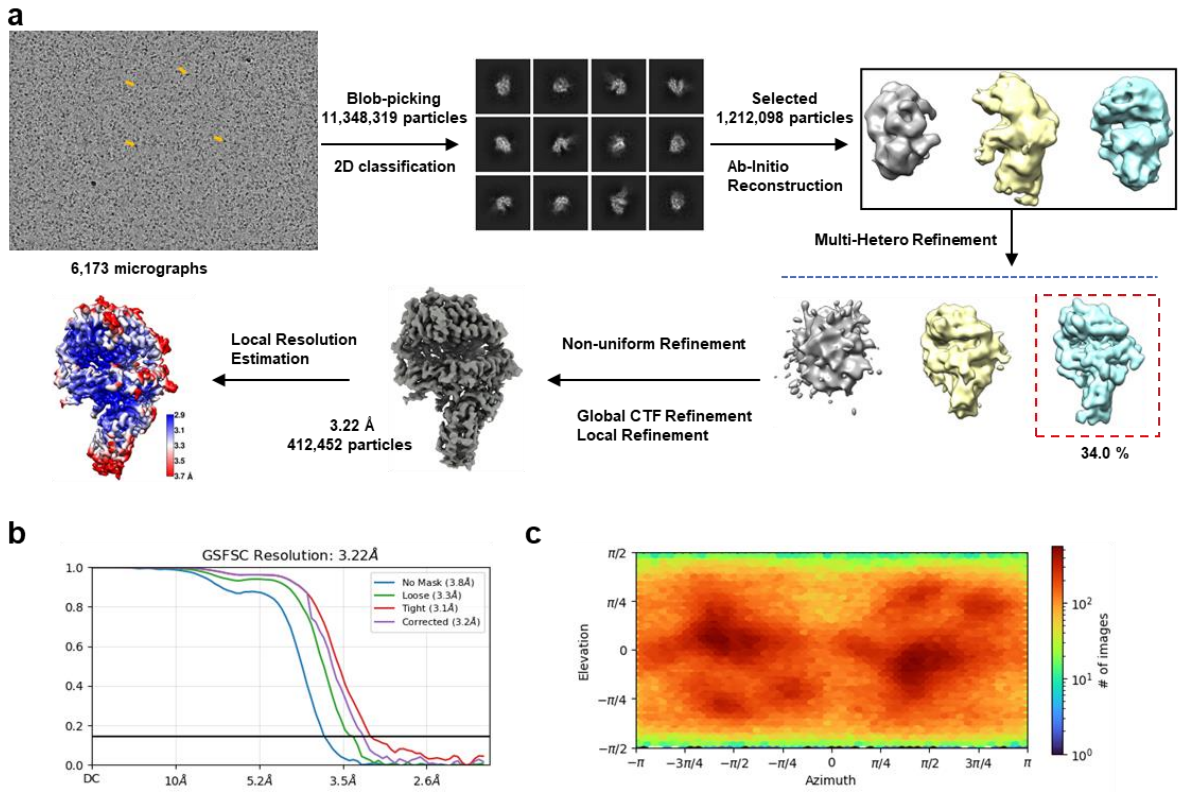

Supplementary information, Figure S10. Cryo-EM data processing pipeline and analysis for the HKU5 RBD–*Ps*PD complex.

(a) Flowchart of Cryo-EM data processing, please see the "Data Processing" section in Materials and Methods for details. (b) Gold standard FSC curve of the HKU5 RBD–*Ps*PD complex is estimated by cryoSPARC. (c) Euler angle distribution of the HKU5 RBD–*Ps*PD complex in the final 3D reconstruction in cryoSPARC.

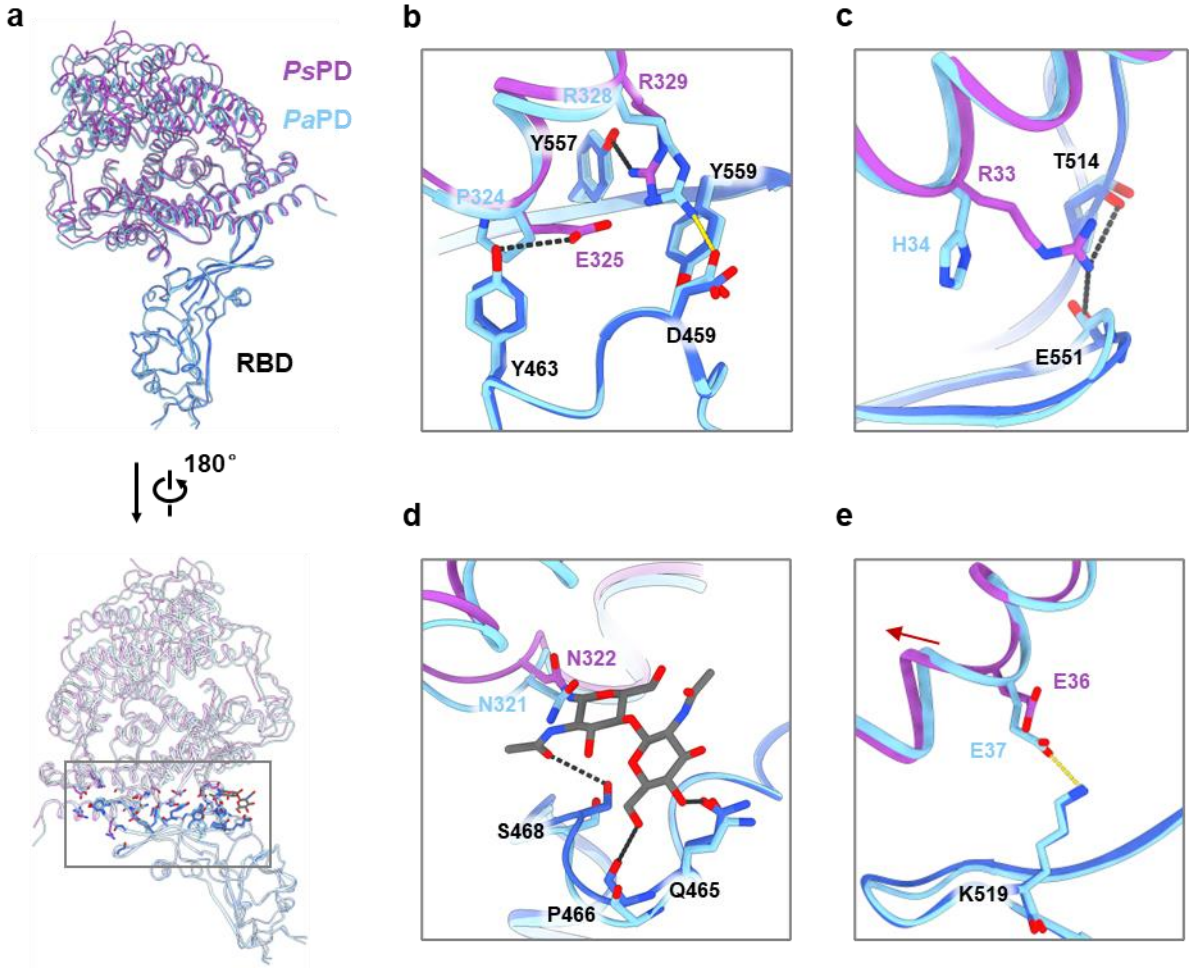

Supplementary information, Figure S11. Comparison of the interfaces between the HKU5 RBD and *Pa*PD or *Ps*PD.

(a) shows an overall structural comparison in different views, with the black box indicating the interaction interface. (b-e) show magnified views of the interface details. In the structural comparison, the RBD and *Ps*PD in the HKU5 RBD–*Ps*PD complex are in purple and marine, respectively. The HKU5 RBD–*Pa*PD complex is in cyan.

Supplementary information, Table S1. Characterization of fatty acids associated with the coronavirus S protein.

Organism	PDB ID	Ligand ID	Ligand Formula	Ligand MW	Ligand Name	Ref.
SARS-CoV-2	6ZB4	EIC	C18 H32 O2	280.445	Linoleic acid	17
SARS-CoV-2	7E7B	ELA	C18 H34 O2	282.461	9-Octadecenoic acid	52
SARS-CoV-2	8H3E	Q83	C15 H18 N2 O5	306.314	7-(6-nitro-2,3-dihydroindol-1-yl)-7-oxidanylidene-heptanoic acid	37
SARS-CoV-2	7Z3Z	STE	C18 H36 O2	284.477	Stearic acid	53
SARS-CoV-2	7Y42	REA	C20 H28 O2	300.435	Retinoic acid	54
SARS-CoV	7ZH1	EIC	C18 H32 O2	280.445	Linoleic acid	55
PCoV_GX	7CN8	EIC	C18 H32 O2	280.445	Linoleic acid	56
HCoV-OC43	7SB5	PLM	C16 H32 O2	256.424	Palmitic acid	35
HCoV-OC43	7SBY	8Z9	C16 H30 O2	254.408	Sapienic acid	
Bat Coronavirus WIV1	8TC0	EIC	C18 H32 O2	280.445	Linoleic acid	
Civet Coronavirus 007	8TC1	EIC	C18 H32 O2	280.445	Linoleic acid	36
Civet Coronavirus SZ3	8TC5	EIC	C18 H32 O2	280.445	Linoleic acid	

Supplementary information, Table S2. Statistics of cryo-EM data collection, processing, and model refinement.

Data collection				
EM equipment	Krios (Thermo Scientific)			
Voltage (kV)	300			
Detector	Gatan K3 Summit			
Energy filter	Gatan GIF Quantum, 20 eV slit			
Pixel size (Å)	1.087			
Electron dose (e-/Å2)	50			
Defocus range (μm)	-1.2 ~ -2.2			
Number of collected micrographs	2,738	3,472	3,103	6,173
Sample	HKU5 S	HKU5 S_{DM}	RBD–*Pa*PD	RBD–*Ps*PD
PDB ID	9KR8	9KR9	9KRA	9KRB
EMDB ID	EMD-62522	EMD-62523	EMD-62524	EMD-62525
3D Reconstruction				
Software	cryoSPARC			
Number of used particles	801,468	40,837	437,582	412,452
Resolution (Å)	2.39	2.80	3.17	3.22
Symmetry	C1			
Map sharpening B factor ($Å^2$)	-91.7	-88.2	-190.3	-187.4
Refinement				
Software	Phenix			
Cell dimensions				
a=b=c (Å)	347.84	347.84	208.704	208.704
α=β=γ (˚)	90			
Model composition				
Protein residues	3,489	3,552	789	796
Sugar	81	87	15	11
Fatty acids	6	3	0	0
R.m.s deviations				
Bonds length (Å)	0.008	0.008	0.006	0.007
Bonds Angle (˚)	1.095	1.012	0.751	0.819
Ramachandran plot statistics (%)				
Preferred	93.49	93.98	93.38	91.79
Allowed	5.96	5.93	6.11	7.95
Outlier	0.55	0.08	0.51	0.25

743 **Supplementary information, Video S1.**

744 Global conformational change from the WT HKU5 S protein to the S_{DM} protein.

745 **Supplementary information, Video S2.**

746 Local conformational change within the S1 subunit of the HKU5 S protein from the WT

747 conformation to the S_{DM} conformation.

748

749